

Reduced-order variational mode decomposition

Zi-Mo Liao¹, Zhiye Zhao¹, Liang-Bing Chen¹, Zhen-Hua Wan^{*1}, Nan-Sheng Liu^{†1}, and Xi-Yun Lu¹

¹Department of Modern Mechanics, University of Science and Technology of China, Hefei 230027, PR China

September 27, 2022

Abstract

A novel data-driven method of modal analysis for complex flow dynamics, termed as reduced-order variational mode decomposition (RVMD), has been proposed, combining the idea of the separation of variables and a state-of-the-art nonstationary signal-processing technique – variational mode decomposition. It enables a low-redundant adaptive extraction of coherent structures in statistically nonstationary flows, with its modes computed by solving an elaborate optimization problem using the block coordinate descent algorithm. Discussion on the intrinsic relations between RVMD and some classic modal decomposition methods demonstrates that RVMD can be reduced into proper orthogonal decomposition (POD) or discrete Fourier transform (DFT) at particular parameter settings. The significant advantages of RVMD for performing time-frequency analysis are highlighted by a signal-processing analogous categorization of the widely-used modal decomposition techniques. It is also confirmed that the combination of RVMD and the Hilbert spectral analysis provides a physically intuitive way to explore the space-time-frequency characteristics of transient dynamics. Finally, all the appealing features of RVMD mentioned above are well verified via two canonical flow problems: the transient cylinder wake and the rectangular turbulent supersonic screeching jet.

*Email address for correspondence: wanzh@ustc.edu.cn

†Email address for correspondence: lns@ustc.edu.cn

Contents

1	Introduction	2
2	Reduced-order variational mode decomposition	4
2.1	Problem formulation	4
2.2	Computing the RVMD modes	8
2.3	Derived eigenvalue problem from RVMD	11
2.4	Criteria for parameters setting	12
3	Relation to existing methods	14
3.1	Proper orthogonal decomposition	14
3.2	Discrete Fourier transformation	15
3.3	Other methods and a signal-processing analogous categorization	15
4	Applications	16
4.1	The transient cylinder wake	17
4.2	The rectangular turbulent supersonic screeching jet	21
4.2.1	Flow configuration	21
4.2.2	Test on the parameters setting	22
4.2.3	RVMD results and discussion	24
5	Conclusion	28
A	Fundamentals in signal processing	29
A.1	Wiener filtering	29
A.2	Analytic signal	29
A.3	Variational mode decomposition	30

1 Introduction

Modal decomposition has become fundamentally important in turbulence research in terms of constructing a low-dimensional representation in the Eulerian perspective and establishing an explicit connection of dynamic process between the physical and phase space (Holmes et al., 2012). Since Lumley (1967, 1970) proposed the proper orthogonal decomposition (POD) in the realm of turbulence, a large variety of modal decomposition methods have been developed for more than 50 years. Coherent structures – organized fluid elements of significant lifetime and scale – can be extracted by these well-designed methods, enabling the mechanistic study of the essential dynamical features inherent in complex flows. Modal analysis has demonstrated its powerful roles in theoretical analysis and engineering applications (Taira et al., 2017, 2020), for example, shedding light on the potential mechanisms of the unsteadiness in shock wave/boundary layer interactions (Priebe et al., 2016), self-similar behaviour in pipe flows (Hellström et al., 2016) and providing insight into the dynamics of large-scale wavepackets in turbulent jets (Schmidt et al., 2018), among others.

Some general consensus has been reached on the direction of the development of modal decomposition, even though various techniques are rooted in different physical considerations and mathematical operations. As proposed by [Noack \(2016\)](#), the first is to extend the information contained in the decomposed modes, and the second is to extract a sparse description of the dominant feature in the original dynamic system ([Brunton et al., 2016](#)). Although increasingly sophisticated experimental techniques and high-performance computing have provided a huge mass of time-accurate flow field data, namely, a prerequisite to explore the transient and intermittent behaviours in statistically nonstationary flows, further development of a mode-based time-frequency analysis framework is still highly desired ([Nekkanti and Schmidt, 2021](#)). It is due to the fact that the conventional construction ideas of existing methods, such as time averaging and linear approximation, limit their ability to characterize the time-frequency information, which motivates us to introduce a new mathematical form of modal expansion to overcome this difficulty.

The two most popular modal analysis techniques, POD and dynamic mode decomposition (DMD, [Schmid, 2010](#)), have demonstrated their good capabilities in a wide range of problems, although various attempts are still raised for their more extensive applications. The core idea of POD is to find an orthonormal basis that spans a finite-dimensional subspace, such that the L^2 -norm of the projected data onto this subspace obtains its maximum in a time (or ensemble) averaged sense ([Holmes et al., 2012](#)). This energetic optimality makes it an efficient way to compress the original data, but the averaging process may result in the loss of the key dynamical information. DMD is proposed to extract modes with temporal monochromaticity through a linear approximation of the original nonlinear system, which can also be regarded as a finite-dimensional approximation of the Koopman operator ([Rowley et al., 2009](#); [Brunton et al., 2022](#)). The eigenvalues and corresponding eigenvectors of the approximated system comprise the DMD modes, whose time coefficients are pure harmonics with exponential growing or decaying. For mean-subtracted data, [Chen et al. \(2012\)](#) have proved that DMD is equivalent to the discrete Fourier transform (DFT). Different from POD, DMD allows us to examine the spectral content of the system in a global manner. Nevertheless, the exponential oscillatory formulation of the time coefficients limits its application to describe general nonstationary processes.

Recently, various time-frequency analysis strategies have been attempted by incorporating concepts in signal processing into the existing modal decomposition methods. [Kutz et al. \(2016\)](#) presented a recursive algorithm called multiresolution DMD, in which the modes with the frequency characteristics localized in time are obtained by a removal-splitting operation. Another interesting attempt was made by [Nekkanti and Schmidt \(2021\)](#) based on the spectral proper orthogonal decomposition (SPOD, [Towne et al., 2018](#)). SPOD is a space-time formulation of POD, which inherits the basic idea of [Lumley \(1967, 1970\)](#). For statistically stationary flows, it computes orthogonal modes that diagonalize the estimated cross-spectral density matrix at each frequency. Two approaches were presented in [Nekkanti and Schmidt \(2021\)](#) to recover the time-frequency contents from the already computed SPOD modes: oblique projection in the time domain and convolution in the frequency domain. These frameworks mentioned above can serve as a good pilot to guide the development of mode-based time-frequency analysis while further efforts are required to improve performance and operability.

In this study, we develop a new data-driven modal analysis method referred to as reduced-order variational mode decomposition (RVMD), which is inspired by the Hilbert-Huang transform (HHT, [Huang et al., 1998](#)) and a state-of-the-art signal-processing technique called vari-

ational mode decomposition (VMD, Dragomiretskiy and Zosso, 2014). It is well known that HHT can provide a feasible path for dealing with nonstationary, nonlinear signals in the Hilbert view (Huang et al., 1999), which is different from the Fourier-based methods such as short-time Fourier transform and wavelet transform. HHT is implemented by decomposing the original time series into intrinsic mode functions (IMFs) and then applying Hilbert spectral analysis to obtain the instantaneous frequencies. As the core concept of HHT, IMFs are usually obtained by empirical mode decomposition or VMD. IMF represents a generalized Fourier expansion that can effectively characterize time-frequency contents with superior resolution (Huang et al., 1999). Drawing on the construction of VMD and combining the idea of the separation of variables, the proposed RVMD can adaptively extract time-frequency features from spatio-temporal data and obtains excellent physical interpretability. The adaptive frequency-domain sparsification is achieved by an iterative optimization using the block coordinate descent algorithm (Wright, 2015), similar to the idea of sparsity-promoting DMD (Jovanović et al., 2014). Note that, the appealing features of RVMD are in line with the outlook in Noack (2016), as the direct results of a mathematically well-defined optimization problem. Two canonical flow problems, i.e., the transient cylinder wake and the rectangular turbulent supersonic screeching jet, are employed to validate the capability of RVMD. It is demonstrated that RVMD not only captures the dominant temporal dynamics accurately but also provides physically meaningful modal information.

The remainder of this paper is organized as follows. Section 2 formulates the proposed method and discusses the properties of computed modes, as well as the criteria for parameters setting. Section 3 elucidates the intrinsic relations between RVMD and various existing methods based on a mathematical perspective, and then presents a signal-processing analogous categorization of different modal techniques. In § 4, two canonical cases are utilized to demonstrate the capabilities and advantages of RVMD. Finally, concluding remarks are summarized in § 5.

2 Reduced-order variational mode decomposition

2.1 Problem formulation

Similar to existing modal decomposition methods, RVMD attempts to find a low-rank variables-separation representation of the observed space-time data $q(\mathbf{x}, t)$ as the following form

$$q(\mathbf{x}, t) = \sum_k \phi_k(\mathbf{x})c_k(t), \quad (1)$$

where $\phi_k(\mathbf{x})$, $\mathbf{x} \in \Omega$ denotes the spatial distribution of the k -th mode and $c_k(t)$, $t \in (-\infty, \infty)$ is the time-evolution coefficient, with Ω denoting the spatial domain over which the flow is defined. Due to the finite energy nature of the flow field, all these functions are square-integrable. Following the formulation of POD (Holmes et al., 2012), we further assume that they belong to the Hilbert space with inner product $\langle \cdot, \cdot \rangle$ and L^2 -norm $\| \cdot \|$ (Zeidler, 2012). Specific definitions of the norm in space and time are

$$\|\phi(\mathbf{x})\|_x \equiv \langle \phi, \phi \rangle_x^{1/2} \quad \text{with} \quad \langle \phi_1(\mathbf{x}), \phi_2(\mathbf{x}) \rangle_x = \int_{\Omega} \phi_1(\mathbf{x})\overline{\phi_2(\mathbf{x})}d\mathbf{x}, \quad (2)$$

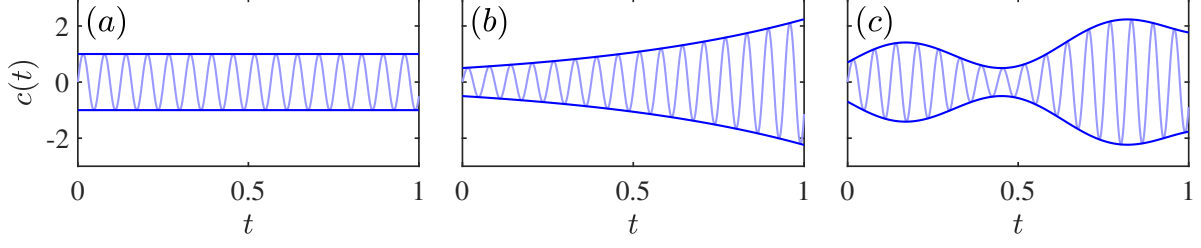


Figure 1: Temporal signals $c(t)$: (a) pure harmonic, (b) pure harmonic with exponential growing, (c) an example of intrinsic mode function. Each signal's upper/lower envelope is indicated using a dark blue curve.

and

$$\|c(t)\|_t \equiv \langle c, c \rangle_t^{1/2} \quad \text{with} \quad \langle c_1(t), c_2(t) \rangle_t = \int_{-\infty}^{\infty} c_1(t) \overline{c_2(t)} dt, \quad (3)$$

respectively. The overline denotes complex conjugate.

The proposed RVMD modes are a group of triplets with a finite number K , written as

$$\{\phi_k(\mathbf{x}), c_k(t), \omega_k\}_{k=1}^K, \quad (4)$$

where ω_k is called the central frequency of $c_k(t)$ that, as shown below, is the averaged frequency weighted by the square of the Fourier transform of the time coefficient $|\hat{c}_k(\omega)|^2$, with $\hat{c}_k(\omega) = \mathcal{F}\{c_k(t)\} = \int_{-\infty}^{\infty} c_k(t) e^{-i\omega t} dt$ and $\hat{\cdot}$ denoting the Fourier transform hereafter. Domains of $\phi_k(\mathbf{x})$, $c_k(t)$, and ω_k are

$$\Phi \equiv \{\phi(\mathbf{x}) \in L^{2,\mathbb{R}}(\Omega) \mid \|\phi(\mathbf{x})\|_{\mathbf{x}} = 1\}, \quad C \equiv L^{2,\mathbb{R}}(-\infty, \infty), \quad \mathbb{R}^+, \quad (5)$$

respectively. Note that, all the components of the RVMD modes are defined in the real domain, ensuring a straightforward flow field reconstruction and a clear physical meaning. Besides, since the spatial distributions are normalized, the energy of each mode can be reflected by its time coefficient, i.e.,

$$E_k = \|c_k(t)\|_t^2. \quad (6)$$

The energy ratio can be further defined to measure the relative strength of each mode

$$\tilde{E}_k \equiv \frac{E_k}{\left(\sum_{i=1}^K E_i\right)}. \quad (7)$$

Before we present the optimization problem that RVMD deals with, it is necessary to introduce the so-called IMF. Since [Huang et al. \(1998\)](#) first proposed the idea of IMF, it has become the central concept of modern nonstationary signal-processing techniques. IMFs are amplitude-modulated-frequency-modulated signals written as:

$$c(t) = A(t) \cos \varphi(t), \quad (8)$$

with non-decreasing phase $\varphi(t)$ and non-negative envelope $A(t)$. Besides, the envelope and the instantaneous frequency $d\varphi/dt$ should vary much slower than the phase ([Gilles, 2013](#);

Daubechies et al., 2011). IMFs can be seen as an extension of the Fourier expansion, while the slow-varying envelope contains information on the temporal evolution (see figure 1). The above definition yields an immediate consequence of limited bandwidth. On the other hand, if an oscillatory signal has a compact bandwidth around a specific frequency in the spectral domain, it will act as an IMF in the time domain. The concept of IMFs enables RVMD to have the expected advantage in describing time-frequency characteristics. In addition, the formulation of RVMD relies on some other fundamental definitions and operations in signal processing, which are given in appendix A.

The core idea of RVMD is to find K modes, as indicated in (4), whose time coefficients are IMFs, providing a low-redundant approximation to the observed field $q(\mathbf{x}, t)$. We achieve this goal by limiting the time coefficient to have a compact bandwidth, rather than explicitly introducing the formulation of IMF (8). In other words, we compute the RVMD modes by minimizing the following two components: the measure of the deviation between the original flow and the mode-reconstructed one, and the sum of the bandwidths of the time-evolution coefficients. The former is expressed as a quadratic penalty term, and the latter is estimated through the squared L^2 -norm of the gradient of $c_k(t)$, as treated in VMD (Dragomiretskiy and Zosso, 2014). The resulting unconstrained optimization problem is given by

$$\min_{\{\phi_k(\mathbf{x}), c_k(t), \omega_k\}_{k=1}^K} \left\{ \alpha \sum_{k=1}^K \left\| \partial_t \left[\left[\left(\delta(t) + i \frac{1}{\pi t} \right) * c_k(t) \right] e^{-i\omega_k t} \right] \right\|_t^2 + \left\| q(\mathbf{x}, t) - \sum_{k=1}^K \phi_k(\mathbf{x}) c_k(t) \right\|_F^2 \right\}, \quad (9)$$

where $\delta(\cdot)$ is the Dirac delta function, $*$ denotes convolution in the time domain. The convolution of $\delta(t) + i/\pi t$ and $c_k(t)$ leads to the analytic representation of $c_k(t)$. An exponential with frequency ω_k is multiplied to shift the mode's frequency spectrum to the baseband, using the frequency shifting property of analytic signals (A.2). We will see later that this manipulation results in a Wiener filtering (A.1) around the central frequency ω_k . The norm $\|f\|_F$ for a given space-time function $f(\mathbf{x}, t)$ in $L^{2, \mathbb{R}}(\Omega) \times L^{2, \mathbb{R}}(-\infty, \infty)$ is defined as

$$\|f(\mathbf{x}, t)\|_F^2 = \int_{\Omega} \int_{-\infty}^{\infty} f(\mathbf{x}, t) \overline{f(\mathbf{x}, t)} dt d\mathbf{x}, \quad (10)$$

which corresponds to the Frobenius norm of matrices. The positive regularization parameter α in (9), referred to as the filtering parameter hereafter, reflects the relative importance of compact bandwidth and accurate reconstruction. The two parameters, α and K , should be input as a priori.

For mathematical simplicity, a spectral-domain alternative of (9) is utilized to compute the RVMD modes. Since the observed data and the RVMD modes are real-valued square-integrable functions, Parseval's theorem can be applied. For two functions $f(t), g(t) \in L^{2, \mathbb{C}}(-\infty, \infty)$, this theorem gives the following identity

$$\int_{-\infty}^{\infty} f(t) \overline{g(t)} dt = \frac{1}{2\pi} \int_{-\infty}^{\infty} \hat{f}(\omega) \overline{\hat{g}(\omega)} d\omega. \quad (11)$$

When $g(t) = f(t)$, (11) turns into

$$\|f(t)\|_t^2 = \frac{1}{2\pi} \|\hat{f}(\omega)\|_\omega^2 \quad \text{with} \quad \|\hat{f}(\omega)\|_\omega^2 = \int_{-\infty}^{\infty} |\hat{f}(\omega)|^2 d\omega. \quad (12)$$

Then, the first term in (9) can be converted into

$$\frac{1}{2\pi} \alpha \sum_{k=1}^K \left\| i\omega [1 + \text{sgn}(\omega + \omega_k)] \hat{c}_k(\omega + \omega_k) \right\|_\omega^2, \quad (13)$$

where $\hat{c}_k(\omega)$ is defined in

$$\hat{C} = \left\{ \hat{c}_k(\omega) \in L^{2,\mathbb{C}}(-\infty, \infty) \mid \hat{c}_k(-\omega) = \overline{\hat{c}_k(\omega)} \right\}. \quad (14)$$

Performing a variable substitution $\omega \leftarrow \omega - \omega_k$, the norm (13) can be written as two times the integral over the non-negative frequencies

$$\frac{1}{2\pi} \sum_{k=1}^K \int_0^{\infty} 4\alpha(\omega - \omega_k)^2 |\hat{c}_k(\omega)|^2 d\omega. \quad (15)$$

Similarly, considering the Hermitian symmetry of real-valued functions, the quadratic penalty term becomes

$$\frac{1}{2\pi} \int_{\Omega} \int_0^{\infty} 2 \left| \hat{q}(\mathbf{x}, \omega) - \sum_{k=1}^K \phi_k(\mathbf{x}) \hat{c}_k(\omega) \right|^2 d\omega d\mathbf{x}. \quad (16)$$

Finally, we get the following optimization problem in the spectral domain, which is equivalent to (9),

$$\min_{\{\phi_k(\mathbf{x}), \hat{c}_k(\omega), \omega_k\}_{k=1}^K} F \left(\{\phi_k(\mathbf{x}), \hat{c}_k(\omega), \omega_k\}_{k=1}^K \right), \quad (17)$$

where the objective function $F(\cdot)$ is

$$\begin{aligned} F \left(\{\phi_k(\mathbf{x}), \hat{c}_k(\omega), \omega_k\}_{k=1}^K \right) &\equiv \\ &\sum_{k=1}^K \int_0^{\infty} 2\alpha(\omega - \omega_k)^2 |\hat{c}_k(\omega)|^2 d\omega \\ &+ \int_{\Omega} \int_0^{\infty} \left| \hat{q}(\mathbf{x}, \omega) - \sum_{k=1}^K \phi_k(\mathbf{x}) \hat{c}_k(\omega) \right|^2 d\omega d\mathbf{x}. \end{aligned} \quad (18)$$

The objective function is to be minimized over all the three components of the RVMD modes in the corresponding feasible regions: $\phi_k(\mathbf{x}) \in \Phi$, $\hat{c}_k(\omega) \in \hat{C}$, and $\omega_k \in \mathbb{R}^+$. The solving process is operated over the positive half of the frequency domain, making use of the Hermitian symmetry, and then the time coefficients $c_k(t)$ can be reconstructed directly. The adaptivity is achieved by optimizing over the central frequencies, thanks to the good mathematical properties of the analytic representation of IMFs. For appropriate parameters setup, RVMD can find modes oscillating around specific frequencies with limited bandwidths, which have (locally) energetic

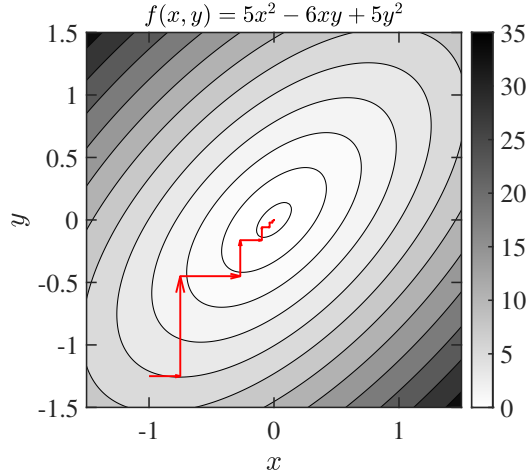


Figure 2: The iteration trajectory of an example problem solved by the coordinate descent algorithm: minimize $f(x, y) = 5x^2 - 6xy + 5y^2$ over the two variables x and y for a given initial value $(x^0, y^0) = (-1, -1.25)$. Sub-minimizations on different coordinates are solved successively: $x^{n+1} = \operatorname{argmin}_x \{f(x, y^n)\}$; $y^{n+1} = \operatorname{argmin}_y \{f(x^{n+1}, y)\}$. As the iteration progresses, (x^n, y^n) approaches the local minimum, which is also the global minimum as f is convex.

dominance compared to the surrounding broadband noise due to turbulent motions and reflect distinctive dynamical properties coherent in space and time.

Moreover, the spatial distribution functions $\phi_k(\mathbf{x})$ are not restricted to be orthogonal in space. Instead, a characteristic scale separation is realized in the time domain (Huang et al., 1999). That is, RVMD inherits the advantages of DMD that the non-orthogonal modes provide the ability to capture the essential dynamical behaviours in systems with non-normal dynamical generators (Trefethen et al., 1993; Schmid, 2007; Jovanović et al., 2014).

2.2 Computing the RVMD modes

Although RVMD adopts an optimization-problem-based framework similar to POD, the former is relatively more complicated to solve. In POD and SPOD, the constructed optimization can be directly converted into an equivalent eigenvalue problem that is easy to solve (Holmes et al., 2012; Towne et al., 2018). To deal with the problem (17), we employ the block coordinate descent (BCD) algorithm described by Liu et al. (2020). The BCD-type algorithms solve a global optimization by successively performing approximate minimization along coordinate hyperplanes. Since the BCD-type algorithms are of efficient performance and easy to implement for handling large-scale non-convex optimization problems, they have been widely applied in computational statistics and machine learning (Wright, 2015). An illustrative example of the coordinate descent algorithm is depicted in figure 2.

To compute the RVMD modes, we first define auxiliary functions as follows

$$F_{\phi_k}^{n+1}(\phi_k) \equiv F\left(\phi_1^{n+1}, \hat{c}_1^{n+1}, \omega_1^{n+1}; \dots; \phi_k, \hat{c}_k^n, \omega_k^n; \dots; \phi_K^n, \hat{c}_K^n, \omega_K^n\right), \quad (19)$$

$$F_{\hat{c}_k}^{n+1}(\hat{c}_k) \equiv F\left(\phi_1^{n+1}, \hat{c}_1^{n+1}, \omega_1^{n+1}; \dots; \phi_k^{n+1}, \hat{c}_k, \omega_k^n; \dots; \phi_K^n, \hat{c}_K^n, \omega_K^n\right), \quad (20)$$

$$F_{\omega_k}^{n+1}(\omega_k) \equiv F\left(\phi_1^{n+1}, \hat{c}_1^{n+1}, \omega_1^{n+1}; \dots; \phi_k^{n+1}, \hat{c}_k^{n+1}, \omega_k; \dots; \phi_K^n, \hat{c}_K^n, \omega_K^n\right), \quad (21)$$

where the superscript $(\cdot)^n$ denotes the current iteration step. Then, the original joint problem, i.e., the minimization over ϕ_k , \hat{c}_k , and ω_k , is decomposed into a sequence of iterative sub-optimizations

$$\phi_k^{n+1} = \operatorname{argmin}_{\phi_k \in \Phi} \left\{ F_{\phi_k}^{n+1}(\phi_k) \right\}, \quad (22)$$

$$\hat{c}_k^{n+1} = \operatorname{argmin}_{\hat{c}_k \in \hat{C}} \left\{ F_{\hat{c}_k}^{n+1}(\hat{c}_k) \right\}, \quad (23)$$

$$\omega_k^{n+1} = \operatorname{argmin}_{\omega_k \in \mathbb{R}^+} \left\{ F_{\omega_k}^{n+1}(\omega_k) \right\}, \quad (24)$$

which can be solved by the calculus of variations.

The corresponding functional for the sub-problem of the spatial distribution $\phi_k(\mathbf{x})$ is

$$J[\phi_k(\mathbf{x})] \equiv \int_{\Omega} \int_0^{\infty} \left| \hat{q}(\mathbf{x}, \omega) - \sum_{i=1}^{k-1} \phi_i^{n+1}(\mathbf{x}) \hat{c}_i^{n+1}(\omega) - \phi_k(\mathbf{x}) \hat{c}_k^n(\omega) - \sum_{i=k+1}^K \phi_i^n(\mathbf{x}) \hat{c}_i^n(\omega) \right|^2 d\omega d\mathbf{x}. \quad (25)$$

To simplify the formulation above, we define the residual function for the k -th mode at iteration step n

$$\hat{r}_k^n(\mathbf{x}, \omega) = \hat{q}(\mathbf{x}, \omega) - \sum_{i=1}^{k-1} \phi_i^{n+1}(\mathbf{x}) \hat{c}_i^{n+1}(\omega) - \sum_{i=k+1}^K \phi_i^n(\mathbf{x}) \hat{c}_i^n(\omega). \quad (26)$$

Let the functional derivative vanish for all variations $\phi_k(\mathbf{x}) + \delta\psi(\mathbf{x}) \in \Phi$, $\delta \in \mathbb{R}$, where ψ is an arbitrary function. Then, we get the necessary condition for extrema

$$\frac{d}{d\delta} \left[\int_{\Omega} \int_0^{\infty} \left| \hat{r}_k^n(\mathbf{x}, \omega) - \phi_k(\mathbf{x}) \hat{c}_k^n(\omega) - \delta\psi(\mathbf{x}) \hat{c}_k^n(\omega) \right|^2 d\omega d\mathbf{x} \right] \Big|_{\delta=0} = 0, \quad (27)$$

which further leads to the following equation

$$0 = \int_{\Omega} \operatorname{Re} \left\{ \int_0^{\infty} \overline{\hat{c}_k^n(\omega)} [\hat{r}_k^n(\mathbf{x}, \omega) - \phi_k(\mathbf{x}) \hat{c}_k^n(\omega)] d\omega \right\} \psi(\mathbf{x}) d\mathbf{x}. \quad (28)$$

Since $\psi(\mathbf{x})$ is an arbitrary function, the fundamental lemma of calculus of variations implies that the rest part in the integrand should be identically zero, i.e.,

$$\operatorname{Re} \left\{ \int_0^{\infty} \overline{\hat{c}_k^n(\omega)} \hat{r}_k^n(\mathbf{x}, \omega) d\omega \right\} = \int_0^{\infty} |\hat{c}_k^n(\omega)|^2 d\omega \phi_k(\mathbf{x}). \quad (29)$$

Let the L^2 -norm of $\phi_k(\mathbf{x})$ be unit, we finally get the update with respect to $\phi_k(\mathbf{x})$

$$\phi_k^{n+1}(\mathbf{x}) = \frac{\operatorname{Re} \left\{ \int_0^\infty \overline{\hat{c}_k^n(\omega)} \hat{r}_k^n(\mathbf{x}, \omega) d\omega \right\}}{\left\| \operatorname{Re} \left\{ \int_0^\infty \overline{\hat{c}_k^n(\omega)} \hat{r}_k^n(\mathbf{x}, \omega) d\omega \right\} \right\|_{\mathbf{x}}}. \quad (30)$$

Similarly, the updates with respect to \hat{c}_k and ω_k become

$$\hat{c}_k^{n+1}(\omega) = \frac{\int_{\Omega} \phi_k^{n+1}(\mathbf{x}) \hat{r}_k^n(\mathbf{x}, \omega) d\mathbf{x}}{1 + 2\alpha(\omega - \omega_k^n)^2}, \quad \omega \geq 0 \quad (31)$$

$$\omega_k^{n+1} = \frac{\int_0^\infty \omega |\hat{c}_k^{n+1}(\omega)|^2 d\omega}{\int_0^\infty |\hat{c}_k^{n+1}(\omega)|^2 d\omega}, \quad (32)$$

respectively.

After deriving the sub-problems we actually solve, the complete algorithm in matrix form for computing the RVMD modes is outlined in the following. The flow data, observed from numerical simulations or experimental measurements, is collected as the data matrix

$$\mathbf{Q} \in \mathbb{R}^{S \times T}, \quad (33)$$

where S and T are the numbers of sampling points in space and time, respectively. Note here, since the flow data is generally nonperiodic in time, a mirror extension is conducted in advance to produce the data matrix. The RVMD modes are represented as column vectors

$$\boldsymbol{\phi}_k \in \mathbb{R}^S, \quad \mathbf{c}_k \in \mathbb{R}^T. \quad (34)$$

Then the DFT is computed, and we only consider the data matrix and the time coefficient vectors on the non-negative part of the frequency domain, which is indicated using the superscript $(\cdot)^+$ as

$$\hat{\mathbf{Q}}^+, \quad \hat{\mathbf{c}}_k^+. \quad (35)$$

The residual matrix for the k -th mode is

$$\hat{\mathbf{R}}_k^+ = \hat{\mathbf{Q}}^+ - \sum_{i \neq k} \boldsymbol{\phi}_i \hat{\mathbf{c}}_i^{+,T}, \quad (36)$$

where the superscript $(\cdot)^T$ denotes the transpose. We then use $(\cdot)^*$ to denote the conjugate and $(\cdot)^H$ to denote the conjugate transpose of matrices and vectors. Another two diagonal matrices are further defined: the non-negative frequency matrix

$$\mathbf{W}^+ = \operatorname{diag}(\boldsymbol{\omega}^+) \quad \text{with} \quad \boldsymbol{\omega}^+ = (\omega_i^+) = (0, 1, 2, \dots, T/2) \times f_s/T, \quad (37)$$

where f_s is the sampling frequency, i.e., the inverse of the sampling interval $1/\Delta t$, and the filtering matrix

$$\hat{\mathbf{G}}_k^+ = \operatorname{diag}(\hat{\mathbf{g}}^+) \quad \text{with} \quad \hat{\mathbf{g}}^+ = (\hat{g}_i^+), \quad \hat{g}_i^+ = \frac{1}{1 + 2\alpha(\omega_i^+ - \omega_k)^2}. \quad (38)$$

The superscripts representing the iteration steps, $(\cdot)^n$ and $(\cdot)^{n+1}$, are omitted for simplicity, but each is implicitly understood as the most recent available update. A C++ implementation of RVMD is available at <https://github.com/ZimoLiao/rvmd-cpp>.

Algorithm (Reduced-order variational mode decomposition, RVMD)

(1) Initialize $\{\phi_k, \hat{c}_k^+, \omega_k\}_{k=1}^K$ and set iteration step $n \leftarrow 0$.

(2) Loop:

Set $n \leftarrow n + 1$, for $k = 1$ to K do:

(a) update the residual matrix for the k -th mode using (36);

(b) update the spatial distribution using

$$\phi_k^{n+1} = \frac{\text{Re} \left\{ \hat{R}_k^+ \hat{c}_k^{+,*} \right\}}{\left\| \hat{R}_k^+ \hat{c}_k^{+,*} \right\|}; \quad (39)$$

(c) update the Fourier transform of the time-evolution coefficient using

$$\hat{c}_k^{+,n+1} = \hat{G}_k^+ \hat{R}_k^{+,T} \phi_k; \quad (40)$$

(d) update the central frequency using

$$\omega_k^{n+1} = \frac{\hat{c}_k^{+,H} \mathbf{W}^+ \hat{c}_k^+}{\hat{c}_k^{+,H} \hat{c}_k^+}; \quad (41)$$

Until convergence:

$$\sum_{k=1}^K \frac{\|\hat{u}_k^{n+1} - \hat{u}_k^n\|_F^2}{\|\hat{u}_k^n\|_F^2} < \epsilon, \quad \hat{u}_k^n \equiv \phi_k^n \hat{c}_k^{+,T,n}, \quad (42)$$

i.e., the iteration difference (the left-hand side) is less than a given tolerance ϵ .

(3) Reconstruct the time-evolution coefficient c_k from \hat{c}_k^+ using the Hermitian symmetry and inverse Fourier transform.

(4) Obtain the RVMD modes $\{\phi_k, c_k, \omega_k\}_{k=1}^K$.

2.3 Derived eigenvalue problem from RVMD

As known, the constrained optimization problem of POD leads to an equivalent eigenvalue problem, which can be easily solved. Next, we will show that a similar eigenvalue problem can be derived from the expressions presented above, revealing how the filtering procedure is accomplished in RVMD. Suppose that the convergence has been achieved, i.e.,

$$\phi_k^{n+1} = \phi_k^n, \hat{c}_k^{n+1} = \hat{c}_k^n, \omega_k^{n+1} = \omega_k^n. \quad (43)$$

We have the filtering function

$$\hat{g}_k(\omega) \equiv 1/[1 + 2\alpha(|\omega| - \omega_k)^2], \quad (44)$$

corresponding to a matrix form $\hat{\mathbf{G}}_k$. In (44), an even extension is carried out to define the filtering function in the whole frequency domain. So multiplying it with the Fourier transform of a real-valued function does not change the Hermitian symmetry of the function.

An alternative to (30) can be formulated as

$$\phi_k^{n+1}(\mathbf{x}) = \frac{\int_{-\infty}^{\infty} \overline{\hat{c}_k^n(\omega)} \hat{r}_k^n(\mathbf{x}, \omega) d\omega}{\left\| \int_{-\infty}^{\infty} \overline{\hat{c}_k^n(\omega)} \hat{r}_k^n(\mathbf{x}, \omega) d\omega \right\|_{\mathbf{x}}}, \quad (45)$$

using the Hermitian symmetry in the spectral domain of the time coefficients and the observed space-time data, i.e., $\hat{c}(\omega) = \hat{c}(-\omega)$ and $\hat{q}(\mathbf{x}, \omega) = \hat{q}(\mathbf{x}, -\omega)$. Then substitute (31) into (45), we obtain the following identity

$$\begin{aligned} \lambda_k \phi_k(\mathbf{x}) &= \int_{-\infty}^{\infty} \hat{g}_k(\omega) \int_{\Omega} \phi_k(\mathbf{x}') \overline{\hat{r}_k(\mathbf{x}', \omega)} d\mathbf{x}' \hat{r}_k(\mathbf{x}, \omega) d\omega \\ &= \int_{\Omega} \left[\int_{-\infty}^{\infty} \hat{g}_k(\omega) \hat{r}_k(\mathbf{x}, \omega) \overline{\hat{r}_k(\mathbf{x}', \omega)} d\omega \right] \phi_k(\mathbf{x}') d\mathbf{x}', \end{aligned} \quad (46)$$

where λ_k is equal to the norm of the right hand side. In matrix form, we have

$$\hat{\mathbf{R}}_k \hat{\mathbf{G}}_k \hat{\mathbf{R}}_k^H \phi_k = \lambda_k \phi_k \quad \text{with} \quad \hat{\mathbf{R}}_k = \hat{\mathbf{Q}} - \sum_{i \neq k} \phi_i \hat{c}_i^T. \quad (47)$$

Notice that Parseval's theorem implies that $\hat{\mathbf{R}}_k \hat{\mathbf{R}}_k^H = 2\pi \mathbf{R}_k \mathbf{R}_k^T$, i.e., the two-point correlation matrix. Hence, RVMD seeks spatial modes that diagonalize the filtered two-point correlation matrix $\hat{\mathbf{R}}_k \hat{\mathbf{G}}_k \hat{\mathbf{R}}_k^H$, while the adaptive sparsification in the frequency domain is achieved through an iterative optimization over the central frequencies.

2.4 Criteria for parameters setting

As aforementioned in §2.3, RVMD leads to an eigenvalue problem (47) for each mode. This understanding provides some basic criteria for selecting the number of modes K and the filtering parameter α in RVMD.

Firstly, consider the most critical input of RVMD – the filtering parameter α . This parameter determines the shape of the filtering function, further affecting the tradeoff between accurate reconstruction and limited bandwidth in RVMD. To estimate an appropriate value of the filtering parameter before performing modal decomposition on specific flow data, we can consider a derived variable, the filter bandwidth Δ , written as

$$\Delta \equiv \sqrt{(2\sqrt{2} - 2)/\alpha}. \quad (48)$$

This is the frequency interval between the two half-power points (cutoff frequencies) of the Wiener filter, following the standard definition of the bandwidth of a bandpass filter. Figure

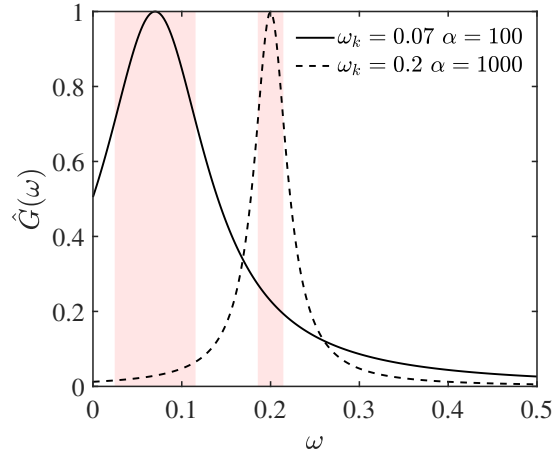


Figure 3: The filtering functions in RVMD with different filtering parameters α and central frequencies ω_k . The bandwidths of the filters are indicated using a light red background.

3 depicts the filtering functions with different α and ω_k , providing an illustration of the introduced parameters. Since the space-time data we handle are discrete, the first rule is that the filter bandwidth Δ should be greater than the frequency resolution of the sampled snapshots. Otherwise, the corresponding α is so large that RVMD is converted into DFT, as we will present in the next section. Another criterion limiting the upper bound on the filter bandwidth is that Δ should be small enough to distinguish different dynamics in the flow. If Δ is too large, e.g., spans the whole frequency domain, the filtered time-evolution coefficient may contain multiple characteristic frequencies like that in POD. Thus, the expected scale separation fails. After the bandwidth's lower and upper bounds are determined, the filtering parameter α can be estimated easily. Secondly, the setting of K is more arbitrary. The number of modes does not alter the adaptivity of RVMD or the dynamical properties of computed modes. So this parameter is merely the expected number of distinctive dynamical behaviours contained in the specific flow.

Finally, since the BCD algorithm can not find the global minimum for the constructed non-convex optimization problem, different central frequencies initialization strategies may lead to different local minimums, i.e., the RVMD modes. When we know very little about the frequency characteristics of the considered flow, initializing the central frequencies to be uniformly or randomly distributed over the entire frequency domain is recommended. In this case, no prior knowledge is required. Furthermore, when a qualitative or quantitative understanding of the frequency characteristics has been established, e.g., through the PSD of the probed temporal sequences or the prediction based on theoretical analysis, a user-defined central frequencies initialization may lead to a better performance – faster convergence, and a smaller number of modes that is enough to capture the dominant dynamics – of the proposed method. A detailed parametric study can be found in § 4.2, practically demonstrating the above discussion on the parameter dependence of RVMD.

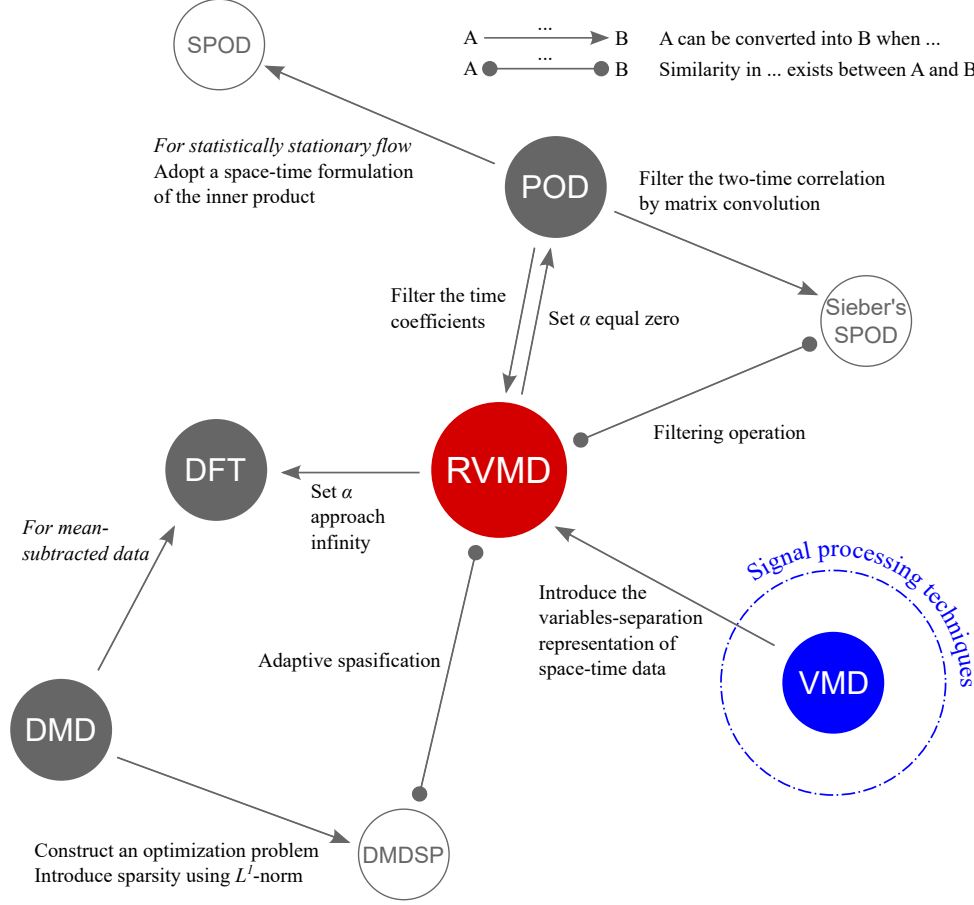


Figure 4: The general relations between RVMD and other methods.

3 Relation to existing methods

This section expounds on the relations between RVMD and some classical modal decomposition methods. We show that RVMD can be converted into POD or DFT at extreme parameter selections. Similarities in construction ideas between RVMD and other widely-used methods are also discussed. Furthermore, to illustrate the advantages of RVMD in performing time-frequency analysis, we briefly introduce the nonstationary signal processing techniques and present a signal-processing analogous categorization of modal decomposition methods. The general relations between RVMD and some other methods are summarized in figure 4.

3.1 Proper orthogonal decomposition

As the filtering parameter α is set as zero, $\hat{\mathbf{G}}_k$ reduces to the identity matrix, then (47) turns into

$$\hat{\mathbf{R}}_k \hat{\mathbf{R}}_k^H \boldsymbol{\phi}_k = 2\pi \mathbf{R}_k \mathbf{R}_k^T \boldsymbol{\phi}_k = \lambda_k \boldsymbol{\phi}_k. \quad (49)$$

If each spatial distribution vector is further restricted to be orthogonal to any other one, we obtain the POD modes directly as a consequence of the reduced version of RVMD. This point can be reached in another way. Specifically, if we drop the bandwidth term and apply an orthogonality

constraint, the original problem (9) becomes

$$\begin{aligned} \min_{\{\phi_k(\mathbf{x}), c_k(t)\}} & \left\{ \left\| q(\mathbf{x}, t) - \sum_{k=1}^K \phi_k(\mathbf{x}) c_k(t) \right\|_{\text{F}}^2 \right\}, \\ \text{s.t.} & \quad \langle \phi_i(\mathbf{x}), \phi_k(\mathbf{x}) \rangle_{\mathbf{x}} = \delta_{ik}. \end{aligned} \quad (50)$$

This problem is equivalent to the following minimization over the spatial distribution functions

$$\begin{aligned} \min_{\{\phi_k(\mathbf{x})\}} & \left\{ \left\| q(\mathbf{x}, t) - \sum_{k=1}^K \frac{\langle \phi_k(\mathbf{x}), q(\mathbf{x}, t) \rangle_{\mathbf{x}}}{\|\phi_k(\mathbf{x})\|_{\mathbf{x}}^2} \phi_k(\mathbf{x}) \right\|_{\text{F}}^2 \right\}, \\ \text{s.t.} & \quad \langle \phi_i(\mathbf{x}), \phi_k(\mathbf{x}) \rangle_{\mathbf{x}} = \delta_{ik}, \end{aligned} \quad (51)$$

which is exactly what POD solves (Holmes et al., 2012).

3.2 Discrete Fourier transformation

The other extreme case is of $\alpha \rightarrow \infty$. In this condition, the only nonzero component of the time coefficient vector $\hat{\mathbf{c}}_k^+$ is exactly the one with the central frequency ω_k , as indicated by (40). In other words, when the filtering parameter α approaches infinity, the time coefficients are pure harmonics, indicating that the RVMD modes reduce to the Fourier modes.

3.3 Other methods and a signal-processing analogous categorization

We have shown that the proposed method would be strictly converted into POD and DFT in two extreme cases. Besides, it is worth noting that RVMD also shares some similarities in the physical considerations or the mathematical operations with various newly developed modal decomposition methods. In the following, we will discuss the relations between RVMD and other methods. Then, a signal-processing analogous categorization is presented to illustrate the capability of each technique.

Since we introduce a filtering term in the constructed optimization problem to obtain limited-bandwidth time coefficients, the optimization procedure finally results in an eigenvalue problem of the filtered two-point correlation matrix (47). A similar idea is adopted in Sieber et al. (2016). Here, we call the method proposed in Sieber et al. (2016) as Sieber's SPOD. Based on the experimental observations on the two-time correlation, Sieber's SPOD computes eigenmodes of a filtered two-time correlation matrix and then obtains time coefficients similar to IMFs. In Sieber's SPOD, the filtering is conducted through a matrix convolution, while RVMD filters the time coefficients directly. Thus, compared to Sieber's SPOD, RVMD presents a mathematically well-defined framework with clearer physical interpretability.

Another essential feature of RVMD is the adaptivity in frequency-domain sparsification. This feature was previously discussed in Jovanović et al. (2014), in which a sparsity-promoting variant of DMD called DMDSF was proposed. In DMDSF, the sparsity is induced by an additional penalty term – L^1 -norm of the vector of DMD amplitudes, while a L^2 -square norm of the gradient of time coefficient is introduced in RVMD to realize this feature. Similarly, RVMD and DMDSF handle a constructed optimization problem to achieve a tradeoff between accurate reconstruction and low-redundant sparse representation.

Category	Signal processing	Modal decomposition
Time-domain analysis		POD
Frequency-domain analysis	FT	DMD, SPOD
Time-frequency analysis	STFT, WT EMD (HHT), VMD	mrDMD RVMD (present)

Table 1: A signal-processing analogous categorization of modal decomposition methods

According to the ability to describe temporal evolution, the existing modal decomposition methods can be generally divided into three categories. This signal-processing analogous categorization is listed in table 1. Since both DMD and SPOD modes oscillate at a single frequency, they can be seen as space-time extensions of the Fourier transform (FT). As we have mentioned above, Fourier-based methods such as short-time Fourier transform (STFT) and wavelet transform (WT) provide frameworks to carry out time-frequency analysis. The multiresolution DMD (mrDMD) lies in this hierarchy, which introduces the idea of wavelet-based multiscale analysis. Although the completeness of mathematics makes the Fourier-based methods widely used and deeply studied, they have to encounter a defect in determining how to select the bases properly as well as the resolution limitation due to the uncertainty principle (also referred to as the Gabor limit). To this end, [Huang et al. \(1998\)](#) proposed a new methodology called Hilbert-Huang transform (HHT) to analyze nonstationary and nonlinear time series in the Hilbert view. The standard HHT decomposes a signal into IMFs using empirical mode decomposition (EMD) and then applies a Hilbert spectral analysis on IMFs to get the instantaneous frequencies. VMD acts as an alternative mathematically well-defined approach for extracting IMFs and performs better than EMD. Since RVMD is a space-time extension of VMD, it inherits the advantages of VMD/EMD in time-frequency representation. RVMD provides an approximate variables-separation representation for space-time data, in which the time-evolution coefficients are IMFs. Based on the idea of HHT, a Hilbert spectral analysis (HSA) can further be performed on the computed RVMD time coefficients, leading to the space-time-frequency characteristics of the original data.

4 Applications

In this section, we apply RVMD to two examples of canonical flow problems: the transient cylinder wake and the rectangular turbulent supersonic screeching jet. The first example is intended to practically introduce the time-frequency analysis framework based on RVMD. The second example is included to demonstrate the applicability of RVMD to complex turbulent flows. The parameter dependence of RVMD is discussed in the latter case to verify the statements we have made in § 2.4.

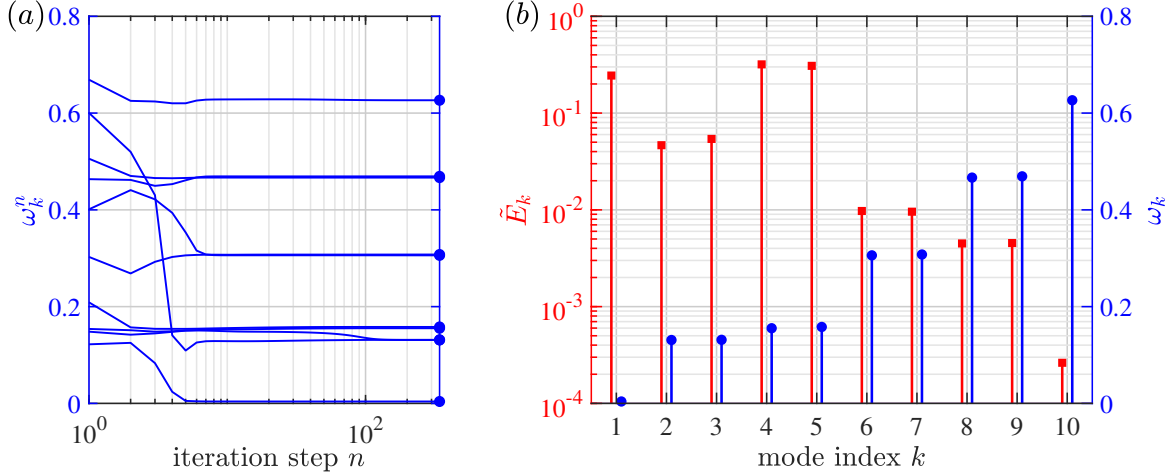


Figure 5: RVMD results for the transient cylinder wake: (a) convergence curve of central frequencies, (b) energy ratios (\tilde{E}_k) and central frequencies (ω_k). For clarity, small shifts are applied to the abscissas in panel b for the plots of \tilde{E}_k and ω_k .

4.1 The transient cylinder wake

We begin with considering the transient cylinder wake, a widely-used problem to validate low-dimensional modelling (Noack et al., 2003; Brunton et al., 2016). A two-dimensional incompressible flow past a cylinder is simulated using a lattice Boltzmann solver. The flow variables are non-dimensionalized by the cylinder diameter D , the inflow velocity U , and the kinetic viscosity ν . We set the Reynolds number $Re = UD/\nu$ equal to 100 to ensure the onset of periodic vortex shedding (Zebib, 1987), similar to the numerical setups in Noack et al. (2016). The origin of coordinates coincides with the center of the cylinder, and the computational domain is set as $(x, y) \in [-10, 15] \times [-10, 10]$. A uniform inflow condition $u = 1, v = 0$ is implemented at the inlet and transverse boundaries, and an extrapolation condition at the outlet boundary. The no-slip boundary condition at the cylinder is imposed by immersed boundary method.

In this simulation, the flow is initially set as the unstable steady state and then gradually evolves to a periodic vortex shedding – known as the von Kármán vortex street, which can be restated in the language of dynamical systems as a transition from the unstable fixed point to the stable limit-cycle oscillation (Zebib, 1987). To include the whole transient process and ensure the time resolution high enough, 600 snapshots of the mean-subtracted velocity fields with sampling interval $\Delta t U/D = 0.25$ are collected to perform modal decomposition. In this case, we set the mode number $K = 10$ and the filtering parameter $\alpha = 1000$, and initialize the central frequencies to be uniformly distributed in the interval $[0, 0.6]$. The setting of empirical parameters follows the criteria proposed in § 2.4. The iterative optimization reaches convergence after 343 steps, with the iteration difference below 0.2%, the convergence curve of the central frequencies ω_k^n are depicted in figure 5(a). The RVMD modes obtained are indexed by their central frequencies from low to high.

A detailed comparative study on different modal decomposition methods has been carried out by Noack et al. (2016), which shows that both POD and DMD can not deal with this problem properly. Since DMD can only capture oscillation modes with exponential envelopes, the intermediate transient process is wiped, indicating a wrong evolutionary trend. POD performs

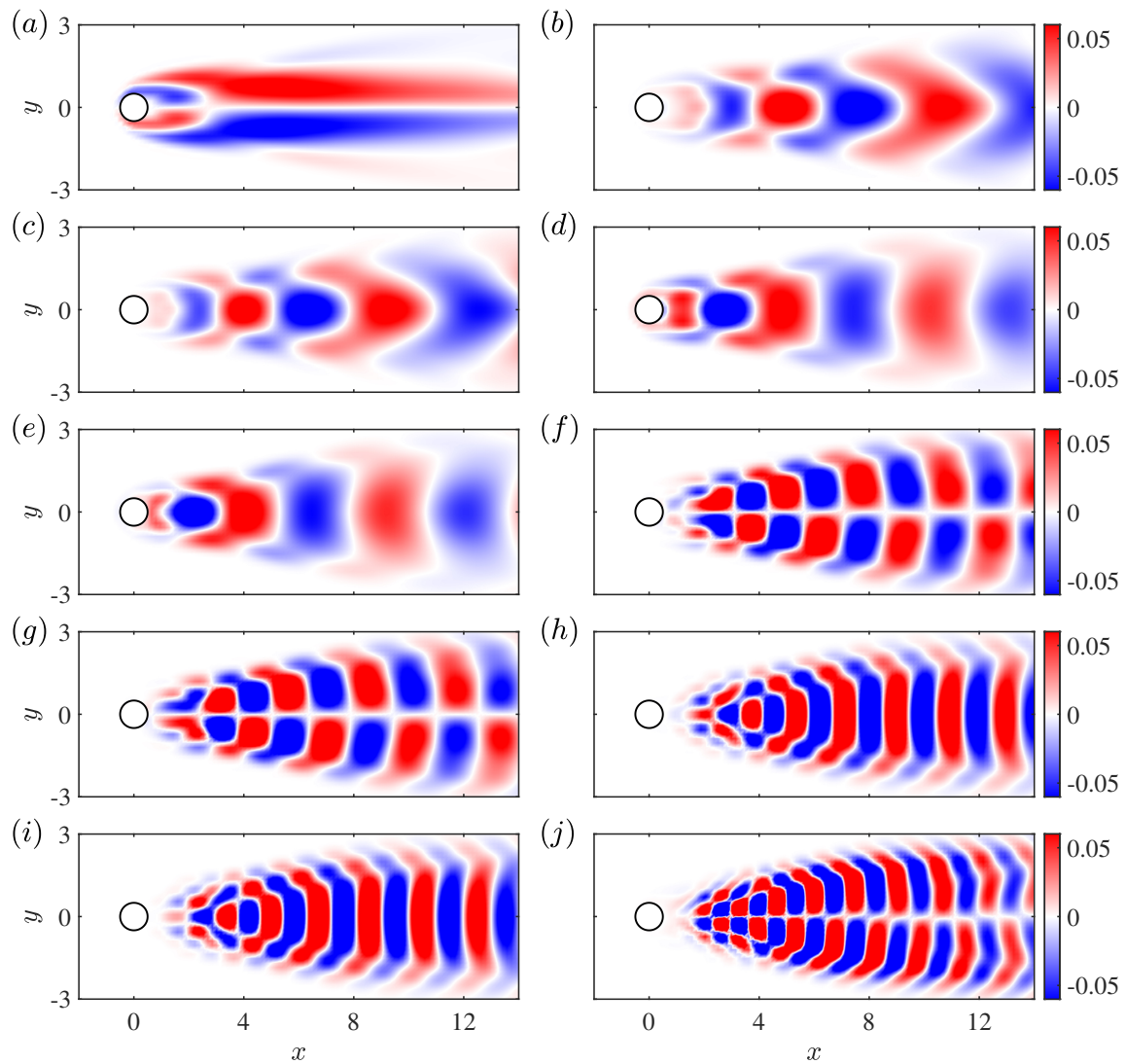


Figure 6: Spatial distributions of the RVMD modes (shown by vorticity) for the transient cylinder wake. We perform a zoom-in to concentrate on the near-wake region plotted for (a-j) modes 1-10.

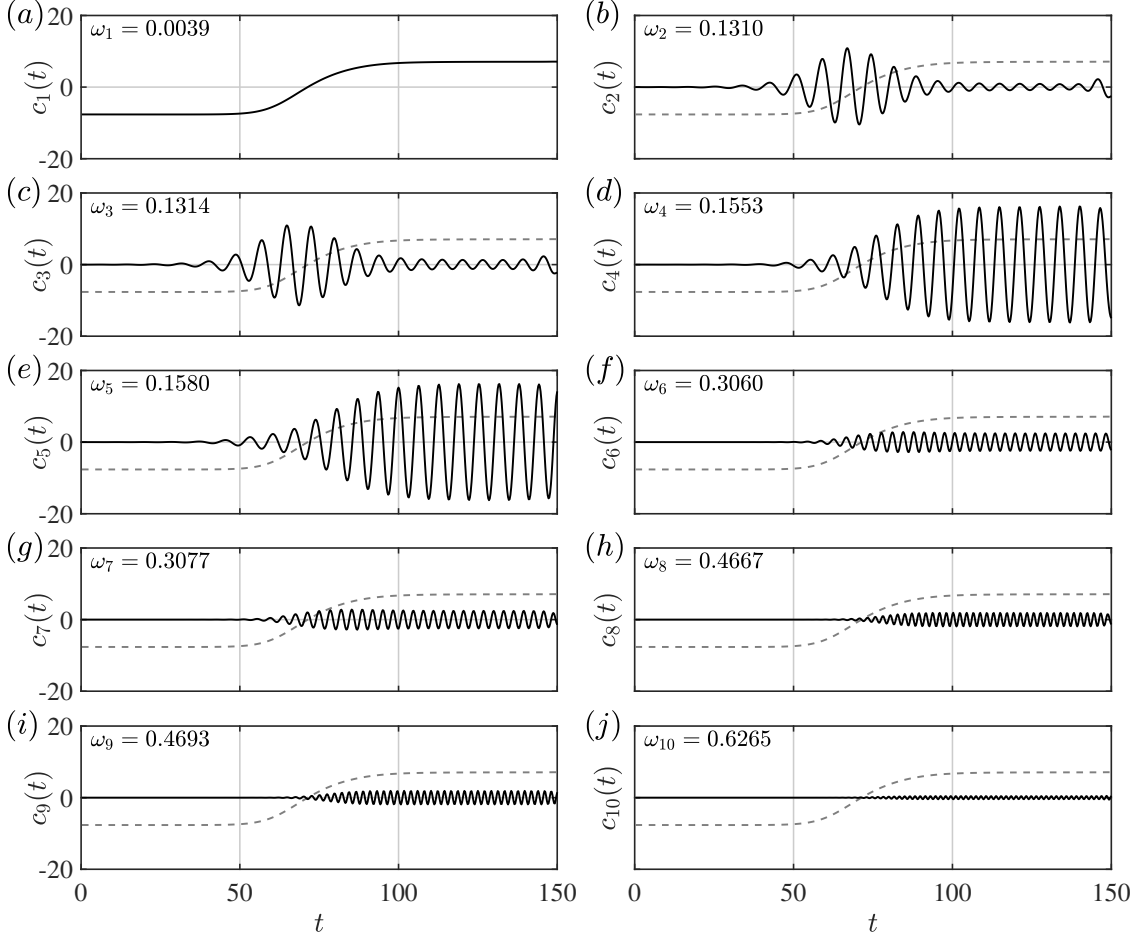


Figure 7: Time-evolution coefficients of the RVMD modes for the transient cylinder wake. (a-j) Modes 1-10. The gray dashed curve indicates the temporal evolution of the shift-mode.

relatively better in extracting the temporal behaviour yet may mix multiple frequencies, leading to confusion in the physical meaning of the modes obtained. The spatial distributions and the corresponding time-evolution coefficients of the RVMD modes are depicted in figures 6 and 7, respectively. The computed modes can be grouped into pairs – the oscillation frequencies and energies of the two modes paired are almost the same, but their phases are different, which is consistent with the previous modal analysis of cylinder wakes (Bagheri, 2013). The post-transient von Kármán vortex street is precisely captured by the first harmonics (modes 4, 5), the second harmonics (modes 6, 7), the third harmonics (modes 8, 9), and the fourth harmonics (mode 10). Mode 1 corresponds to the so-called shift-mode reported by Noack et al. (2003), defined as the transient from the initially steady solution to the post-transient time-averaged flow. It should be emphasized that due to the limited-bandwidth property of the RVMD modes, there is no spurious oscillation mixed in the temporal evolution of the shift-mode (see figure 7(a)).

Another intriguing finding is that RVMD resolves the intermediate vortex shedding, as shown in figure 6(b, c) and figure 7(b, c). The mode pair's central frequency $\omega_{2,3} \approx 0.131$ matches the results of linear stability analysis (Noack et al., 2003), in which the predicted frequency is 0.135.

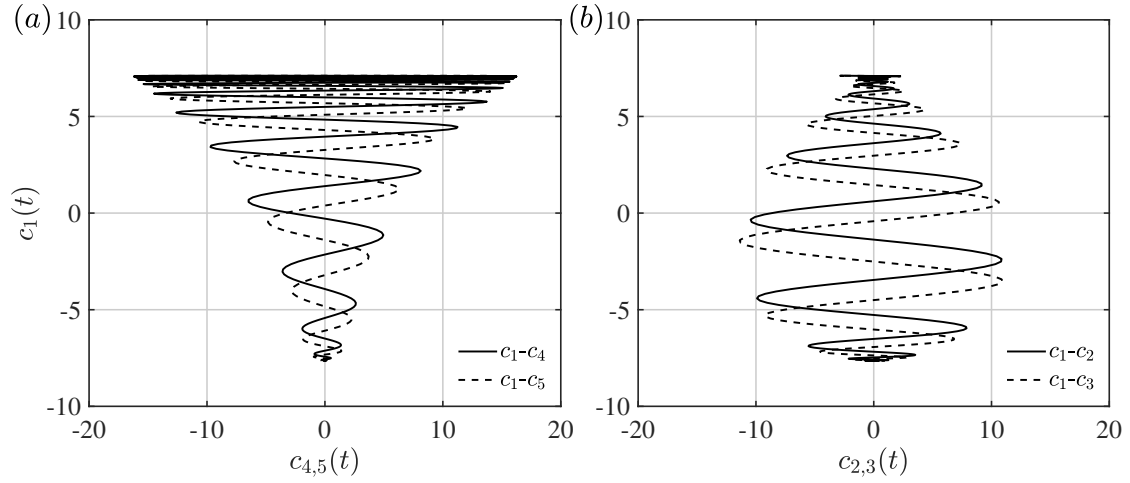


Figure 8: The transient trajectory in RVMD coordinates. The shift-mode versus (a) the periodic vortex shedding modes, (b) the transient linear stability modes.

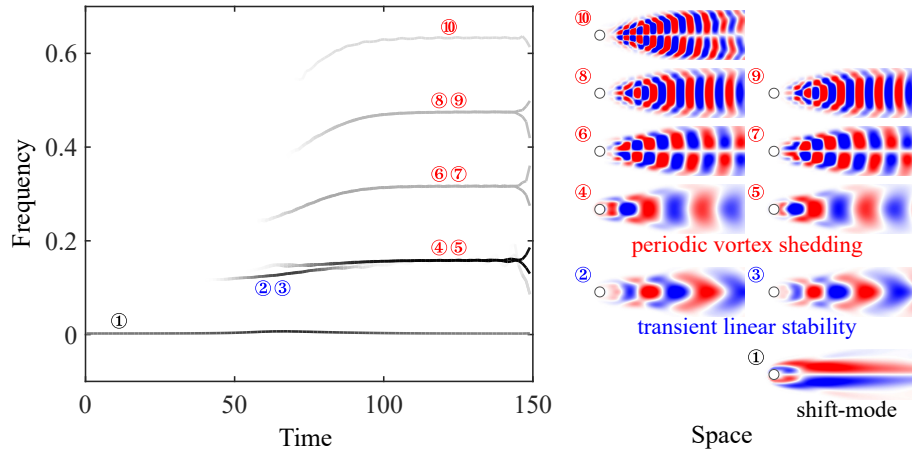


Figure 9: The Hilbert spectrum of the time-evolution coefficients and the corresponding spatial distributions. In the Hilbert spectrum, the curve of each RVMD mode is grey-scaled by its energy that evolves in the time-frequency plane, with darker for higher energy. At the end of the time axis, an abrupt increase or decrease of frequency arises for each RVMD mode due to the end effects inherent in computing the Hilbert spectrum (Huang et al., 1998), other than the physical evolution dynamics.

Two significant differences exist between the transient linear stability modes (modes 2, 3) and the periodic vortex shedding modes (modes 4, 5). First, the maximum fluctuation of transient linear stability modes is far from the cylinder, while the maximum fluctuation of vortex shedding modes nears the cylinder, as shown in figure 6(b-e). Second, while the transient linear stability modes experience a growing-peaking-decaying process, the vortex shedding modes have a later onset and finally reach a stable-oscillation state. As illustrated in figure 8, the trajectories of the transient cylinder wake in RVMD coordinates, i.e., curves $c_1-c_{4,5}$ and $c_1-c_{2,3}$ display totally different evolution characteristics. This observation indicates that the distinguishment of the two behaviours may be critical to describing the whole flow process, further affecting the predictive power of the constructed low-dimensional model (Noack et al., 2003). Compared to existing methods (Siegel et al., 2008; Noack et al., 2016), RVMD can provide an empirical expansion for the transient cylinder wake with the best physical interpretability. Each distinctive behaviour – namely shift-mode, transient linear stability modes, and periodic vortex shedding modes – is captured and isolated, avoiding frequency mixing. These results further confirm the advantages of spatially non-orthogonal modes in capturing dynamical characteristics.

After extracting the IMF-like time coefficients by RVMD, we can further perform a Hilbert spectral analysis to get the space-time-frequency characteristics of the transient cylinder wake. The analytic representations of the real-valued time coefficients $c_k(t)$ are considered as

$$c_{A,k}(t) = c_k(t) + i\mathcal{H}c_k(t) = A_k(t)e^{i\varphi_k(t)}, \quad (52)$$

where the operator \mathcal{H} denotes the Hilbert transform, $A_k(t)$ is the envelope, and $\varphi_k(t)$ is the phase (see appendix A.2). The instantaneous frequency is defined as $d\varphi_k(t)/dt$. The Hilbert spectrum is depicted in figure 9. By combining RVMD and HSA, we get a picture that indicates the temporal dynamics in a physically intuitive way. A one-to-one correspondence exists between the spatial distribution and the evolution curve in the time-frequency plane of each RVMD mode, providing a sparse and powerful description of the transient dynamics.

4.2 The rectangular turbulent supersonic screeching jet

4.2.1 Flow configuration

Here, we take the rectangular supersonic screeching jet as a typical example to demonstrate the applicability of RVMD in practical turbulent flows. Since Powell (1953) first detected the discrete-frequency high-energy screech in underexpanded supersonic jets, many efforts have been devoted to describing, explaining, and predicting this phenomenon. Understanding the key characteristics and the underlying mechanisms in screeching jets is crucial for aeroacoustic theory and aerospace engineering. However, the complex flow processes – shear-induced turbulence, shock cells, and their nonlinear interactions – make it hard to reveal the origin of screech and present reliable predictions. In recent years, data-driven modal analysis has provided a new perspective to quantify and interpret this phenomenon (Jovanović et al., 2014; Li et al., 2021; Edgington-Mitchell et al., 2022).

We use data obtained via a high fidelity implicit large eddy simulation (ILES) on a Cartesian grid (Ye et al., 2020). This ILES was performed using an in-house compressible flow solver HiResX. All the variables are non-dimensionalized using the nozzle height h , the fully expanded jet velocity U_j , the far-field pressure p_∞ and density ρ_∞ , and the reference dynamic viscosity μ_∞ .

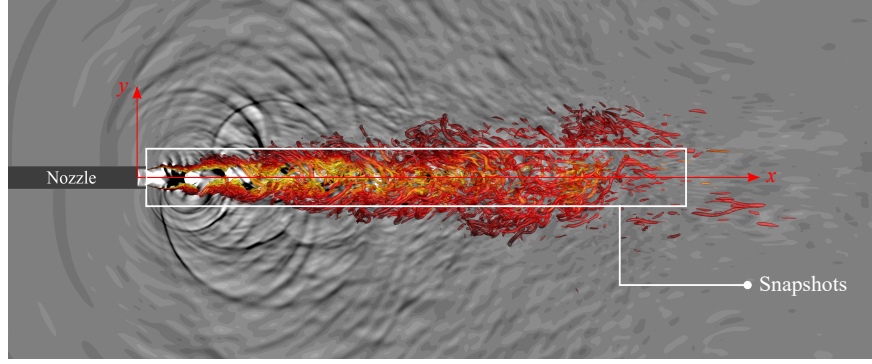


Figure 10: Flow configuration of the rectangular turbulent supersonic screeching jet. The vortex structures are shown by the Q -criterion (colored by the streamwise velocity), and the divergence of velocity is contoured as the background.

The jet operates at the nozzle pressure ratio $NPR = 2.09$ and a fully-expanded Mach number $M_j \equiv U_j/a_j = 1.55$. The far-field sound speed and the jet sound speed are $a_\infty \approx 339$ m/s and $a_j \approx 278$ m/s, respectively. Since the spanwise boundaries of this simulation are periodic, the three-dimensional effect is relatively weak. The calculated shock-cell spacing ($L_s \approx 2.51h$) and the fundamental screech tone (Strouhal number $St_s = \omega_s h/U_j = 0.114$) agree well with previous experimental measurements (Raman and Rice, 1994; Panda et al., 1997) and LES data (Berland et al., 2007). Details on numerical setups can be found in Ye et al. (2020). 1600 snapshots of the fluctuating pressure are sampled in the streamwise-transverse plane with a dimensionless time interval $\Delta t U_j/h = 0.1$ to perform modal analysis. A rectangle domain $(x, y) \in [0.6h, 35.2h] \times [-1.86h, 1.86h]$ is chosen to contain the shock cells and the surrounding shear layers, as shown in figure 10.

4.2.2 Test on the parameters setting

A detailed study on the parameters setting of RVMD is performed first to further verify our statements in § 2.4. We will quantitatively assess the dependence of the RVMD results on the two inputs, i.e., the number of modes K and the filtering parameter α , and how the initialization strategies of the central frequencies (corresponding to Strouhal number $St_k \equiv \omega_k h/U_j$ hereafter) affect the RVMD results.

By theory, each RVMD mode can be seen as an eigenvector of the filtered two-point correlation matrix, and the filtering function is determined by α as

$$\frac{1}{1 + 2\alpha(\omega - \omega_k)^2}. \quad (53)$$

This filter provides a prior spectrum of the time coefficient $c_k(t)$ with bandwidth $\Delta = [(2\sqrt{2} - 2)/\alpha]^{1/2}$ around ω_k . To illustrate the dependence on α (i.e., Δ), ten trials are presented at the same number of modes ($K = 24$) and the same initialization of the central frequencies (uniformly distributed in the whole frequency domain). The values of the filtering parameters and the corresponding bandwidths are listed in table 2.

As indicated in figure 11, a proper choice of α is crucial for the expected properties of RVMD: the ability to capture finite-bandwidth dynamics and the adaptivity in extracting the

α	100	300	1000	3000	10000	30000	100000	300000	1000000	3000000
Δ (points)	145.63	84.08	46.05	26.59	14.56	8.41	4.61	2.66	1.46	0.84

Table 2: The filtering parameters and the corresponding filter bandwidths (in sampling points).

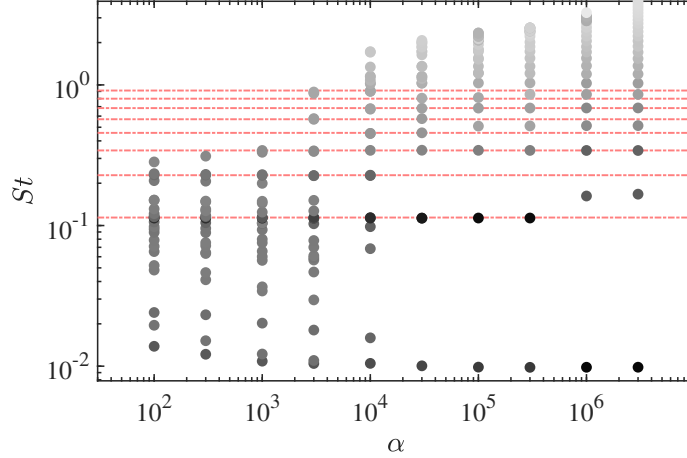


Figure 11: RVMD modes for the rectangular screeching jet at different filtering parameters α . The marked point of each RVMD mode is grey-scaled by its energy ratio, i.e., darker for higher energy. The red dash-dot lines indicate the fundamental screech tone $St_s = 0.114$ and its harmonics.

characteristic frequencies. For large α (i.e., small Δ), the adaptivity is dropped, and the iterative algorithm finally obtains the Fourier modes at the given initial central frequencies. For small α (i.e., large Δ), RVMD reduces to POD as expected. In this case, the local energetic dominant behaviours at relatively high frequencies are neglected, and a large amount of the RVMD modes represent low-frequency broadband behaviours that are difficult to interpret in flow physics. This adaptive modal decomposition realizes its best performance when we set α around 10000. RVMD precisely captures the high-energy harmonic modes of jet screeching. Meanwhile, some low-frequency dynamics are extracted by RVMD. We will show later that these modes reveal an oscillatory stretching of the shock cell and may affect the amplitudes of the screeching modes. Although the filtering parameter is indeed flow-problem dependent, it has been shown here that a proper choice can be easily made post hoc, as in VMD (Dragomiretskiy and Zosso, 2014).

Figure 12(a) displays the results of RVMD with the same filtering parameters ($\alpha = 10000$), the same initialization of the central frequencies (uniformly distributed in the whole frequency domain), but different numbers of modes K . The adaptivity of RVMD is again proved in these trials obtained. The modes that oscillate around the fundamental screech tone are always captured. For larger K , more harmonics and low-frequency dynamics are successively resolved. In figure 12(b), we depict the RVMD results with different K , for which the central frequencies are initialized to be quadratically distributed in the frequency domain. It is evident that compared with the result in figure 12(a), RVMD is more likely to extract the characteristic modes with relatively lower frequencies in this case, which is consistent with the prior assumption we have made in initializing the central frequencies.

According to the above discussion, we set the filtering parameter $\alpha = 10000$ and the number

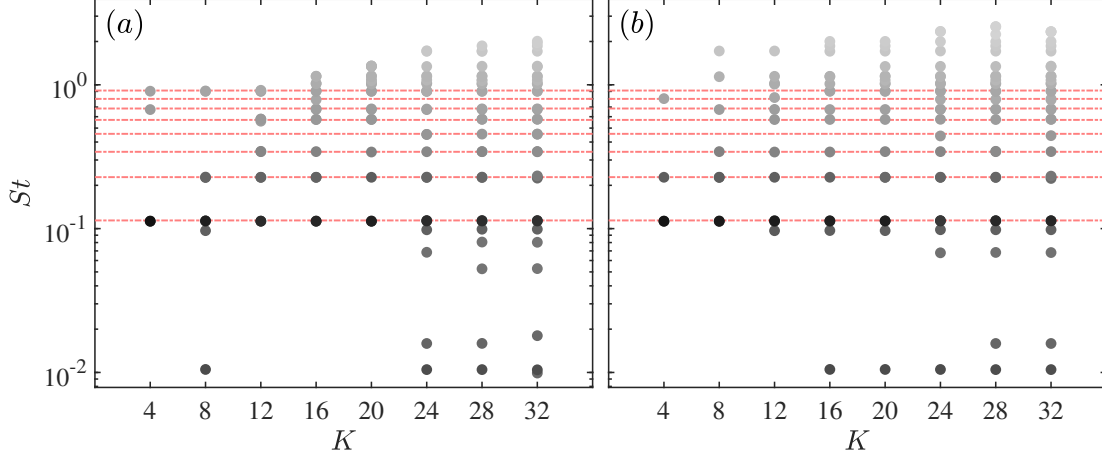


Figure 12: RVMD modes for the rectangular screeching jet using the same filtering parameters $\alpha = 10000$ but different numbers of modes K . The central frequencies are initialized to be (a) uniformly, (b) quadratically distributed in the frequency domain.

of modes $K = 24$ in the next subsection to ensure that dominant dynamic processes at various time scales are well captured. The central frequencies are initialized as uniformly distributed in the whole frequency domain, which means that no prior knowledge is required.

4.2.3 RVMD results and discussion

The energy ratios and central frequencies (namely, St_k) of the RVMD modes are given in figure 13. The fundamental screech tone ($St_s \approx 0.114$) and its harmonics are also marked using horizontal light-blue line segments. As expected, the RVMD modes precisely capture the flow processes that characterize the screeching phenomena. The first two harmonics, which are also the most energetic screeching modes, are resolved by two mode pairs (modes 5, 6 and modes 7, 8). As described in the previous case, a mode pair consists of two modes for which the central frequencies and the energies contained are very close. Figure 14 shows the maximum cross-correlation and the phase lag between the RVMD modes. The maximum cross correlation between time coefficients $c_{k'}(t)$ and $c_k(t)$ is defined as

$$R_{k'k} = \frac{\max_{\tau} \int_{-\infty}^{\infty} c_k(t) c_{k'}(t + \tau) dt}{\sqrt{\int_{-\infty}^{\infty} |c_k(t)|^2 dt} \sqrt{\int_{-\infty}^{\infty} |c_{k'}(t)|^2 dt}}, \quad (54)$$

and the corresponding phase lag is

$$\Delta\phi_{k'k} = \omega_k \tau, \quad \tau = \operatorname{argmax}_{\tau} \left\{ \int_{-\infty}^{\infty} c_k(t) c_{k'}(t + \tau) dt \right\}. \quad (55)$$

These two variables further quantitatively reveal the properties of the so-called mode pair. Both R_{56} and R_{78} exceed 0.95, and the phase lag between the two modes in each pair is around a quarter $|\Delta\phi_{56}| \approx |\Delta\phi_{78}| \approx 1/4$ like the Fourier modes $\sin \omega t$ and $\cos \omega t$. In addition to the screeching modes, some low-frequency energetic modes (modes 1, 2) are obtained, whose

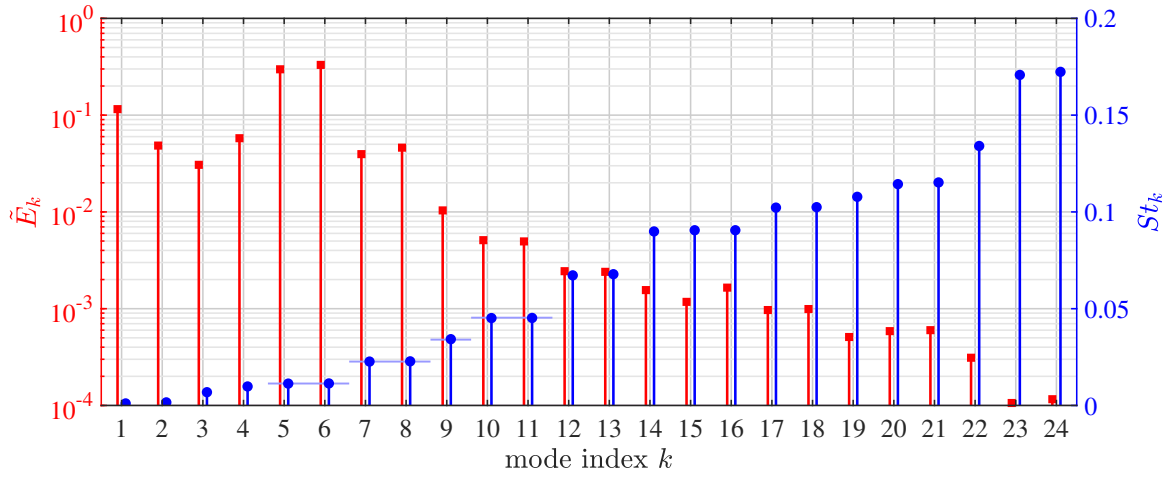


Figure 13: RVMD results for the rectangular screeching jet: energy ratios (\tilde{E}_k) and central frequencies (plotted as St_k).

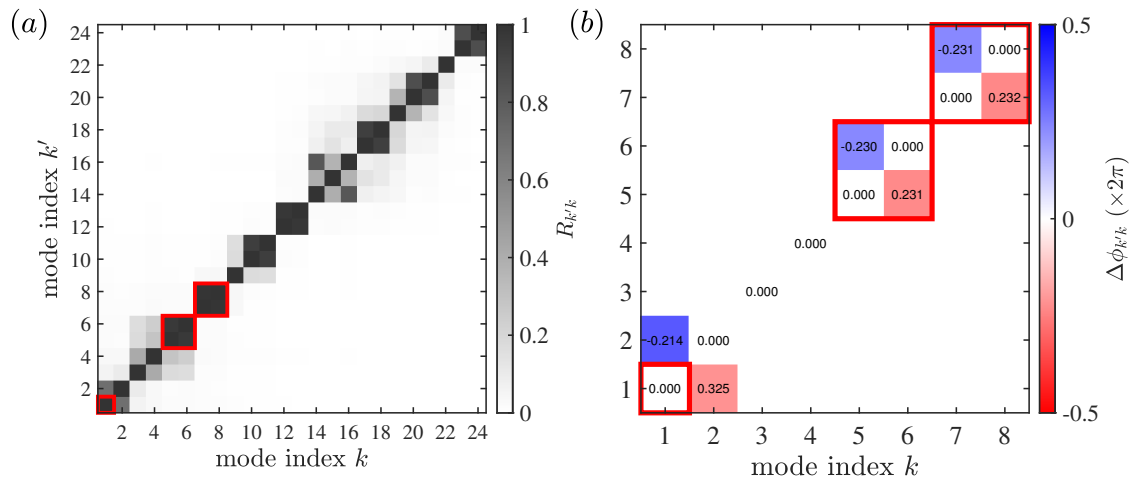


Figure 14: (a) The maximum cross-correlation and (b) the phase lag between each RVMD mode.

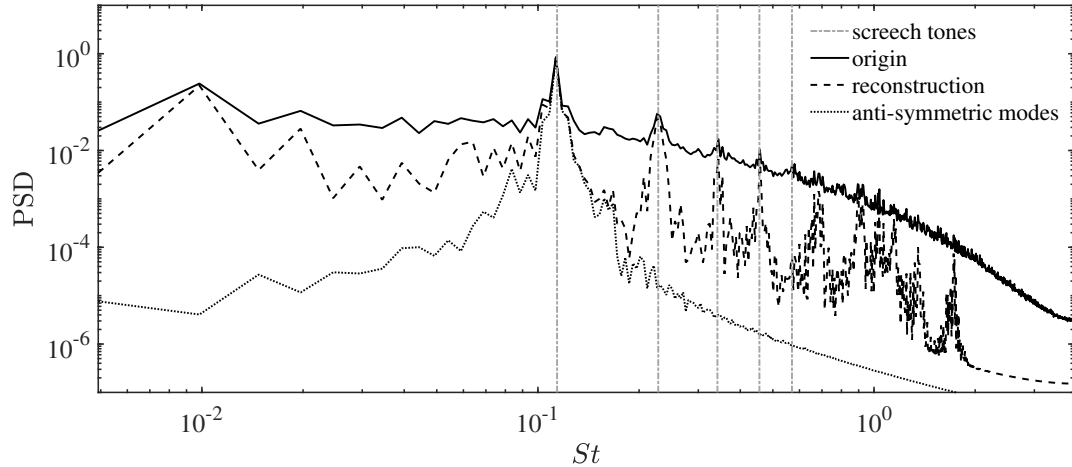


Figure 15: Spatially averaged PSD of the rectangular screeching jet.

central frequencies are one order of magnitude lower than the fundamental screech tone. These low-frequency characteristics are also found in the power spectral density (PSD) of the pressure fluctuations close to the nozzle lip (Berland et al., 2007). The spatially averaged PSD of the rectangular turbulent supersonic screeching jet and the spectrum reconstructed by the RVMD modes are depicted in figure 15. The reconstructed PSD clearly shows the frequency-domain sparsification property of RVMD – the distinctive dynamic properties are adaptively captured while the surrounding broadband noise (fluctuation) induced by turbulence is dropped.

Figure 16 shows the spatial distributions of the RVMD modes. The fundamental screeching modes (5, 6) are anti-symmetric, indicating a flapping behaviour of the jet. The second-order screeching modes (7, 8) are symmetric, indicating a nonflapping ‘varicose’ structure. The spatially averaged PSD of the flow reconstructed by the anti-symmetric mode pair is shown in figure 15, displaying a significant energetic dominance. These decomposed modes are in good agreement with the experimental observations in Raman and Rice (1994). In Raman’s work, the symmetry properties of the two screeching modes are inferred from the phase lag between pressure signals detected by a pair of microphones symmetrically arranged. Another property of the spatial distribution apart from the difference in symmetry is that the anti-symmetric modes span the entire shock-cell region, while the symmetric modes are localized around the first two/three shock cells. This spatial locality is much more pronounced for higher-order harmonic modes, as seen in figure 16(*i-x*). Convective wavepacket structures can be found within the shear layers on both sides of the first shock cell. When the shear layers impinge the first normal shock, the high-frequency pressure fluctuation will radiate outwards other than directly penetrating the shock to travel downstream.

Interestingly, it is found in figure 16(*a, b*) that the two aforementioned low-frequency modes (1, 2) actually represent an oscillatory stretching of the shock cell in the streamwise direction. The energy of these two modes is lower than the anti-symmetric modes but slightly higher than the symmetric modes (see figure 13), which means that this low-frequency feature should not be ignored when we consider the screeching phenomena in rectangular supersonic jets. In previous studies on screeching jets, the shock cell spacing is always treated as constant in time, forming the basis for predicting screech tones and amplitudes. Since IMFs are amplitude-modulated-

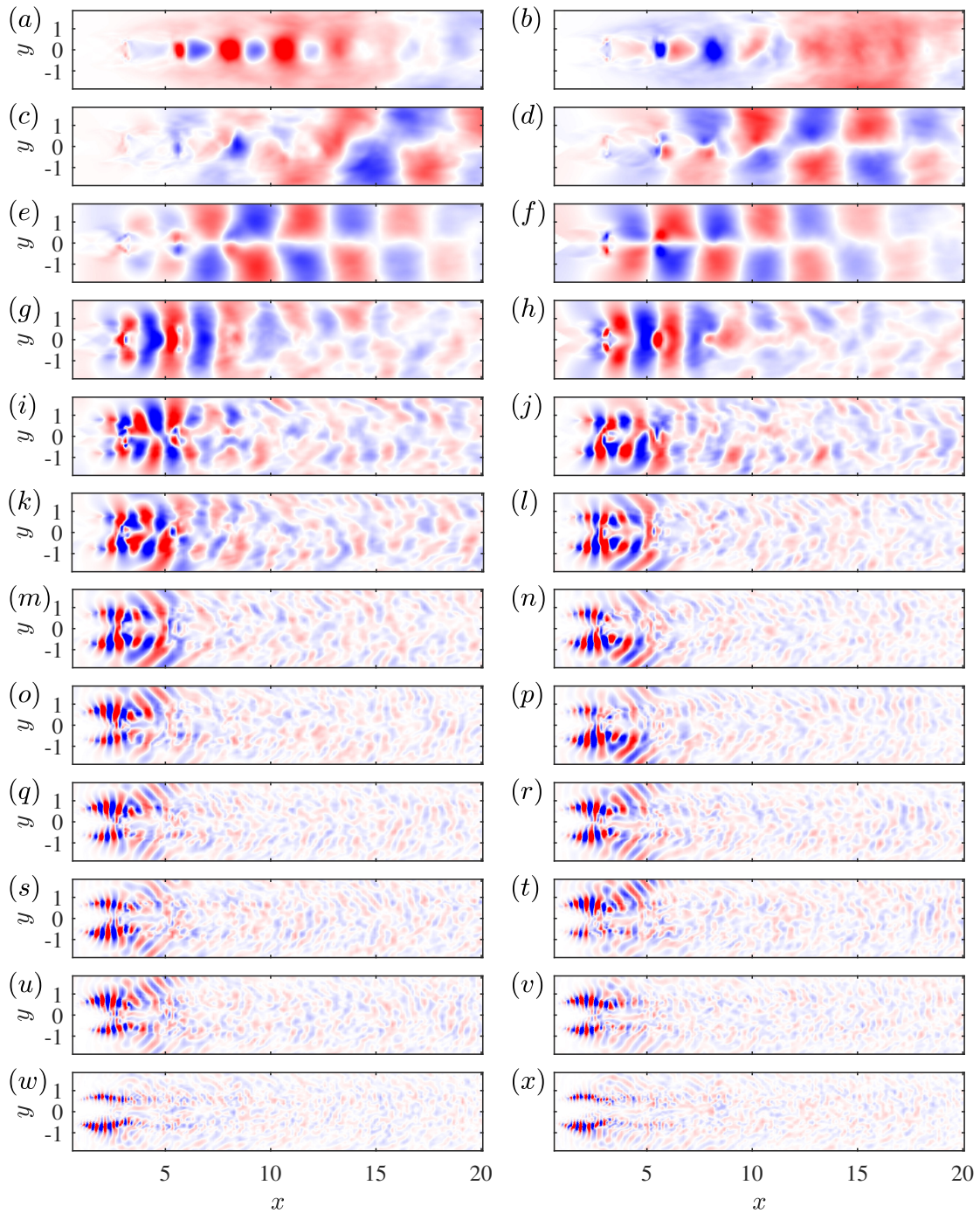


Figure 16: Spatial distributions of RVMD modes for the rectangular screeching jet. (a-x) Modes 1-24.

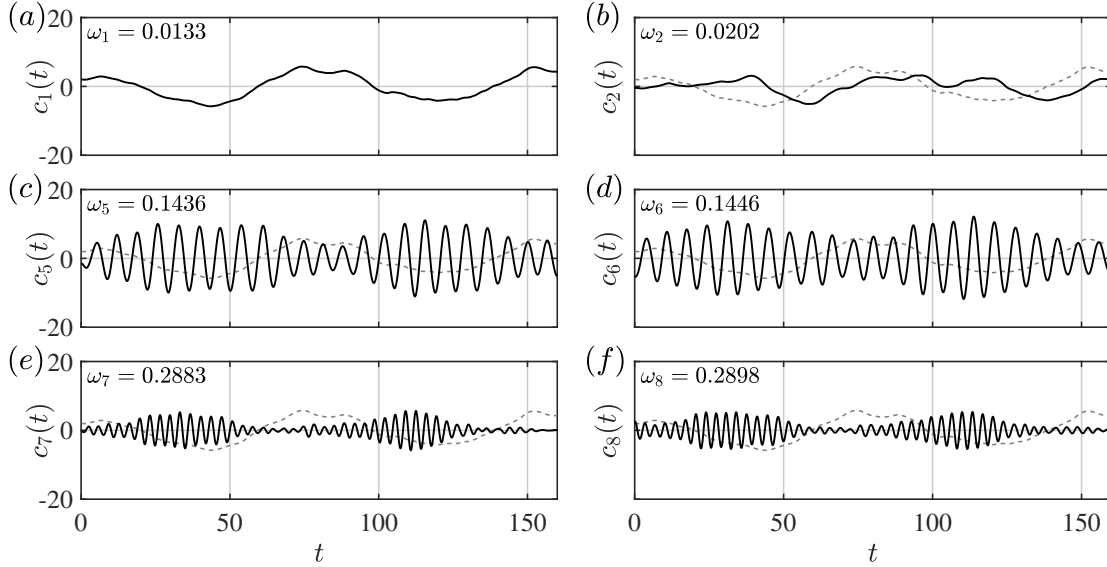


Figure 17: Selected time-evolution coefficients of RVMD modes for the rectangular screeching jet. (a-b) Modes 1-2, (c-f) modes 5-8.

frequency-modulated signals, the temporal evolution of mode strength can be obtained in RVMD modes. As depicted in figure 17(c-f), the envelopes of the first two screeching modes show similar oscillatory behaviour with the shock cell stretching (a), suggesting an intriguing interaction between the low-frequency shock-cell motion and the relatively high-frequency screeching behaviours. This amplitude modulation phenomenon can also be found in the previous simulation of Berland et al. (2007), indicated by the pressure history close to the nozzle lip. In this work, RVMD gives us an intuitive glimpse into the physical mechanism of this phenomenon. This discovery may advance the understanding and modelling of self-sustaining processes in rectangular screeching jets.

5 Conclusion

In this study, a novel data-driven modal analysis technique termed as reduced-order variational mode decomposition (RVMD) is proposed, which enables a low-redundant adaptive extraction of coherent structures in complex flows. The most significant advantage of this method over the existing ones is that the time-frequency information is inherently included in the RVMD modes, drawing on the concept of intrinsic mode functions in signal processing. Hence, the RVMD modes can provide a sparse representation of the observed space-time data with excellent physical interpretability.

RVMD can be regarded as the combination of the variables-separation modes and VMD, whose modes are computed by solving a minimization problem using the block coordinate descent algorithm. We prove that RVMD can be reduced to POD as the filtering parameter α equals zero and to DFT as α approaches infinity, bridging the energetic optimality and the single-frequency property. The most critical difference between RVMD and existing methods is the rich information contained in the time-evolution coefficients in IMF form. Thus, RVMD offers a

succinct framework for performing time-frequency analysis on statistically nonstationary flows. A further combination of RVMD and the Hilbert spectral analysis can provide an intuitive picture of the space-time-frequency coherency of the considered flows. The properties mentioned above of RVMD have been illustrated in two canonical flow problems: the transient cylinder wake and the rectangular turbulent supersonic screeching jet. In both cases, RVMD demonstrates its adaptivity in frequency-domain sparsification. Besides, the intermediate transient processes, the linear stability modes, and the amplitude modulation phenomenon across time scales, etc., are resolved by the RVMD modes, confirming that it is a physically illuminating method.

Since RVMD is mathematically well-defined and easy to implement, further developments and applications are expected. Specifically, potential applications of this method include modal reduction of complex flows with transient behaviours, analysis of the temporal evolution and physical processes in statistically nonstationary flows, crossing-scale amplitude/frequency modulation analysis in wall turbulence, and multi-variate signal processing of fluid dynamics.

A Fundamentals in signal processing

A.1 Wiener filtering

Here, we introduce some essential concepts in signal processing. At first, consider an observed temporal signal $f_0(t)$ consisting of the original signal $f(t)$ and a zero-mean Gaussian noise η . The inverse problem of recovering the original signal from observed data can be addressed by Tikhonov regularization, which leads to a minimization problem

$$\min_f \{ \|f - f_0\|^2 + \alpha \|\partial_t f\|^2 \}, \quad (56)$$

where $\|\cdot\|$ denotes the L^2 -norm, α is a prior parameter to control the bandwidth of the filter below. We can solve this problem through a standard variational procedure, leading to a Wiener filtering on observed data

$$\hat{f}(\omega) = \frac{1}{1 + \alpha\omega^2} \hat{f}_0(\omega), \quad (57)$$

This simple optimization problem forms the basis of VMD and the proposed RVMD.

A.2 Analytic signal

For the convenience of mathematics, a regular manipulation is to convert the real-valued signal into a corresponding analytic representation in complex domain through Hilbert transform. The so-called analytic signal is defined as

$$c_A(t) = c(t) + i\mathcal{H}c(t), \quad (58)$$

where $i = \sqrt{-1}$ is the imaginary unit, and \mathcal{H} denotes the Hilbert operator. The Hilbert transform of $c(t)$ is a linear operator defined as the Cauchy principal value (denoted by p.v.) of the convolution with $1/\pi t$

$$\mathcal{H}c(t) = \frac{1}{\pi} \text{p.v.} \int_{-\infty}^{\infty} \frac{c(\tau)}{t - \tau} d\tau. \quad (59)$$

The Hilbert transform maps cosine functions to their corresponding sine functions, leading to an important property of the constructed analytic signal, unilateral spectrum (i.e., has no negative frequency components). In particular for IMF defined as (8), Bedrosian's theorem (Bedrosian, 1963) implies that

$$c_A(t) = A(t)[\cos \varphi(t) + i \sin \varphi(t)] = A(t)e^{i\varphi(t)}. \quad (60)$$

Another useful property of analytic signal is that multiplying it with a pure exponential results in a simple frequency shifting

$$c_A(t)e^{-i\omega_0 t} \xleftrightarrow{\mathcal{F}} \hat{c}_A(\omega) * \delta(\omega + \omega_0) = \hat{c}_A(\omega + \omega_0), \quad (61)$$

where $*$ denotes convolution, and $\delta(\cdot)$ is the Dirac delta function. Equation (61) stems from the basic modulation property of Fourier transform.

A.3 Variational mode decomposition

The basic idea of variational mode decomposition (VMD, Dragomiretskiy and Zosso, 2014) is to decompose the observed one-component real-valued signal $f(t)$ into K sub-signals $u_k(t)$, namely modes, such that

- (1) The linear superposition of the K modes reconstructs the input;
- (2) The bandwidth of each mode is as compact as possible. In other words, each mode is supposed to oscillate around a specific central frequency ω_k .

A constrained optimization problem can be constructed based on the two goals above and combined with the concepts outlined previously

$$\begin{aligned} \min_{\{u_k(t), \omega_k\}} & \left\{ \sum_{k=1}^K \left\| \partial_t \left[\left(\delta(t) + i \frac{1}{\pi t} \right) * u_k(t) \right] e^{-i\omega_k t} \right\|^2 \right\}, \\ \text{s.t.} & \quad \sum_{k=1}^K u_k(t) = f(t), \end{aligned} \quad (62)$$

As the formulation in Wiener filtering (56), the squared L^2 -norm of the gradient is the bandwidth estimation of each mode. The convolution of $\delta(t) + i/\pi t$ and $u_k(t)$ leads to the corresponding analytic representation of $u_k(t)$. An exponential of the carrier frequency ω_k is multiplied to shift the mode's frequency spectrum to the baseband, transforming the original low-pass filter (57) into a narrow-band filter around ω_k .

References

- S. Bagheri. Koopman-mode decomposition of the cylinder wake. *J. Fluid Mech.*, 726:596–623, 2013. doi: 10.1017/jfm.2013.249.
- E. Bedrosian. A product theorem for Hilbert transforms. *Proc. IEEE*, 51(5):868–869, 1963. doi: 10.1109/proc.1963.2308.

- J. Berland, C. Bogey, and C. Bailly. Numerical study of screech generation in a planar supersonic jet. *Phys. Fluids*, 19(7):075105, 2007. doi: 10.1063/1.2747225.
- S. L. Brunton, J. L. Proctor, and J. N. Kutz. Discovering governing equations from data by sparse identification of nonlinear dynamical systems. *Proc. Natl. Acad. Sci.*, 113(15):3932–3937, 2016. doi: 10.1073/pnas.1517384113.
- S. L. Brunton, M. Budisić, E. Kaiser, and J. N. Kutz. Modern Koopman theory for dynamical systems. *SIAM Rev.*, 64(2):229–340, 2022. doi: 10.1137/21m1401243.
- K. K. Chen, J. H. Tu, and C. W. Rowley. Variants of dynamic mode decomposition: boundary condition, Koopman, and fourier analyses. *J. Nonlinear Sci.*, 22(6):887–915, 2012. doi: 10.1007/s00332-012-9130-9.
- I. Daubechies, J.-F. Lu, and H.-T. Wu. Synchrosqueezed wavelet transforms: an empirical mode decomposition-like tool. *Appl. Comput. Harmon. Anal.*, 30(2):243–261, 2011.
- K. Dragomiretskiy and D. Zosso. Variational mode decomposition. *IEEE Trans. Signal Process.*, 62(3):531–544, 2014. doi: 10.1109/Tsp.2013.2288675.
- D. Edgington-Mitchell, X.-R. Li, N.-H. Liu, F. He, T. Y. Wong, J. Mackenzie, and P. Nogueira. A unifying theory of jet screech. *J. Fluid Mech.*, 945:A8, 2022. doi: 10.1017/jfm.2022.549.
- J. Gilles. Empirical wavelet transform. *IEEE Trans. Signal Process.*, 61(16):3999–4010, 2013. doi: 10.1109/tsp.2013.2265222.
- L. H. O. Hellström, I. Marusic, and A. J. Smits. Self-similarity of the large-scale motions in turbulent pipe flow. *J. Fluid Mech.*, 792, 2016. doi: 10.1017/jfm.2016.100.
- P. Holmes, J. L. Lumley, G. Berkooz, and C. W. Rowley. *Turbulence, coherent structures, dynamical systems and symmetry*. Cambridge University Press, 2nd edition, 2012.
- N. E. Huang, Z. Shen, S. R. Long, M. C. Wu, H. H. Shih, Q.-N. Zheng, N.-C. Yen, C. C. Tung, and H. H. Liu. The empirical mode decomposition and the Hilbert spectrum for nonlinear and non-stationary time series analysis. *Proc. R. Soc. A: Math. Phys. Eng. Sci.*, 454(1971): 903–995, 1998.
- N. E. Huang, Z. Shen, and S. R. Long. A new view of the nonlinear water waves: the Hilbert spectrum. *Annu. Rev. Fluid Mech.*, 31:417–457, 1999. doi: 10.1146/annurev.fluid.31.1.417.
- M. R. Jovanović, P. J. Schmid, and J. W. Nichols. Sparsity-promoting dynamic mode decomposition. *Phys. Fluids*, 26(2):024103, 2014. doi: 10.1063/1.4863670.
- J. N. Kutz, X. Fu, and S. L. Brunton. Multiresolution dynamic mode decomposition. *SIAM J. Appl. Dyn. Syst.*, 15(2):713–735, 2016. doi: 10.1137/15m1023543.
- X.-R. Li, N.-H. Liu, P.-F. Hao, X.-W. Zhang, and F. He. Screech feedback loop and mode staging process of axisymmetric underexpanded jets. *Exp. Therm. Fluid Sci.*, 122:110323, 2021.

- H.-Y. Liu, J. Hu, Y.-F. Li, and Z.-W. Wen. *Optimization: modeling, algorithm and theory (in Chinese)*. Higher Education Press, 2020.
- J. L. Lumley. The structure of inhomogeneous turbulent flows. In A. M. Yaglom and V. I. Tatarski, editors, *Atmospheric turbulence and radio wave propagation*, pages 166–178, Nauka, 1967.
- J. L. Lumley. *Stochastic tools in turbulence*. Academic Press, 1970.
- A. Nekkanti and O. T. Schmidt. Frequency-time analysis, low-rank reconstruction and denoising of turbulent flows using spod. *J. Fluid Mech.*, 926:A26, 2021. doi: ARTNA2610.1017/jfm.2021.681.
- B. R. Noack. From snapshots to modal expansions - bridging low residuals and pure frequencies. *J. Fluid Mech.*, 802:1–4, 2016. doi: 10.1017/jfm.2016.416.
- B. R. Noack, K. Afanasiev, M. Morzyński, G. Tadmor, and F. Thiele. A hierarchy of low-dimensional models for the transient and post-transient cylinder wake. *J. Fluid Mech.*, 497:335–363, 2003. doi: 10.1017/s0022112003006694.
- B. R. Noack, W. Stankiewicz, M. Morzynski, and P. J. Schmid. Recursive dynamic mode decomposition of transient and post-transient wake flows. *J. Fluid Mech.*, 809:843–872, 2016. doi: 10.1017/jfm.2016.678.
- J. Panda, G. Raman, and K. Zaman. Underexpanded screeching jets from circular, rectangular and elliptic nozzles. In *3rd AIAA/CEAS Aeroacoustics Conference*, page 1623, 1997.
- A. Powell. On the mechanism of choked jet noise. *Proc. Phys. Soc.*, 66(12):1039, 1953.
- S. Priebe, J. H. Tu, C. W. Rowley, and M. P. Martín. Low-frequency dynamics in a shock-induced separated flow. *J. Fluid Mech.*, 807:441–477, 2016. doi: 10.1017/jfm.2016.557.
- G. Raman and E. J. Rice. Instability modes excited by natural screech tones in a supersonic rectangular jet. *Phys. Fluids*, 6(12):3999–4008, 1994. doi: 10.1063/1.868389.
- C. W. Rowley, I. Mezić, S. Bagheri, P. Schlatter, and D. S. Henningson. Spectral analysis of nonlinear flows. *J. Fluid Mech.*, 641:115–127, 2009. doi: 10.1017/s0022112009992059.
- P. J. Schmid. Nonmodal stability theory. *Annu. Rev. Fluid Mech.*, 39(1):129–162, 2007. doi: 10.1146/annurev.fluid.38.050304.092139.
- P. J. Schmid. Dynamic mode decomposition of numerical and experimental data. *J. Fluid Mech.*, 656:5–28, 2010. doi: 10.1017/S0022112010001217.
- O. T. Schmidt, A. Towne, G. Rigas, T. Colonius, and G. A. Brès. Spectral analysis of jet turbulence. *J. Fluid Mech.*, 855:953–982, 2018. doi: 10.1017/jfm.2018.675.
- M. Sieber, C. O. Paschereit, and K. Oberleithner. Spectral proper orthogonal decomposition. *J. Fluid Mech.*, 792:798–828, 2016. doi: 10.1017/jfm.2016.103.

- S. G. Siegel, J. Seidel, C. Fagley, D. M. Luchtenburg, K. Cohen, and T. McLaughlin. Low-dimensional modelling of a transient cylinder wake using double proper orthogonal decomposition. *J. Fluid Mech.*, 610:1–42, 2008. doi: 10.1017/s0022112008002115.
- K. Taira, S. L. Brunton, S. T. M. Dawson, C. W. Rowley, T. Colonius, B. J. McKeon, O. T. Schmidt, S. Gordeyev, V. Theofilis, and L. S. Ukeiley. Modal analysis of fluid flows: an overview. *AIAA J.*, 55(12):4013–4041, 2017. doi: 10.2514/1.J056060.
- K. Taira, M. S. Hemati, S. L. Brunton, Y. Y. Sun, K. Duraisamy, S. Bagheri, S. T. M. Dawson, and C. A. Yeh. Modal analysis of fluid flows: applications and outlook. *AIAA J.*, 58(3): 998–1022, 2020. doi: 10.2514/1.J058462.
- A. Towne, O. T. Schmidt, and T. Colonius. Spectral proper orthogonal decomposition and its relationship to dynamic mode decomposition and resolvent analysis. *J. Fluid Mech.*, 847: 821–867, 2018. doi: 10.1017/jfm.2018.283.
- L. N. Trefethen, A. E. Trefethen, S. C. Reddy, and T. A. Driscoll. Hydrodynamic stability without eigenvalues. *Science*, 261(5121):578–584, 1993. doi: doi:10.1126/science.261.5121.578.
- S. J. Wright. Coordinate descent algorithms. *Math. Program.*, 151(1):3–34, 2015. doi: 10.1007/s10107-015-0892-3.
- C.-C. Ye, P.-J.-Y. Zhang, Z.-H. Wan, D.-J. Sun, and X.-Y. Lu. Numerical investigation of the bevelled effects on shock structure and screech noise in planar supersonic jets. *Phys. Fluids*, 32(8):086103, 2020. doi: 10.1063/5.0013263.
- A. Zebib. Stability of viscous flow past a circular cylinder. *J. Eng. Math.*, 21(2):155–165, 1987. doi: 10.1007/bf00127673.
- E. Zeidler. *Applied functional analysis: applications to mathematical physics*. Springer Science & Business Media, 2012.